

Philipp Sauter

Correlation of separatrix density with turbulence parameters and electron-ion heat exchange

**IPP 2022-01
Januar 2022**

EBERHARD KARLS
UNIVERSITÄT
TÜBINGEN



Correlation of separatrix density with turbulence parameters and electron-ion heat exchange

Philipp Sauter

A thesis presented for the degree of
Master of Science

Eberhard-Karls Universität Tübingen
Max-Planck-Institut für Plasmaphysik

01.12.2021



Max-Planck-Institut
für Plasmaphysik

(This page is intentionally left blank)

Masterarbeit im Fach Physik
Eberhard-Karls-Universität Tübingen
Mathematisch-Naturwissenschaftliche Fakultät
Physikalisches Institut

Autor:

Philipp Sauter, B.Sc.
Geboren am 1.12.1996 in Stuttgart
Matrikelnummer: 4018519

Akademische Betreuer:

Prof. Dr. Josef Jochum
Eberhard-Karls-Universität Tübingen
Prof. Dr. Rudolf Neu
Max-Planck-Institut für Plasmaphysik Garching

Fachliche Betreuer:

Dr. Thomas Eich
Dr. Dominik Brida
Max-Planck-Institut für Plasmaphysik Garching

Wintersemester 2021/22

(This page is intentionally left blank)

Hiermit versichere ich nach § 17 Abs. 4 des Allgemeinen Teils der Prüfungsordnung für den Masterstudiengang Physik der Universität Tübingen, dass ich die Arbeit selbstständig verfasst, keine anderen als die angegebenen Hilfsmittel und Quellen benutzt, alle wörtlich oder sinngemäß aus anderen Werken übernommene Aussagen als solche gekennzeichnet habe und dass die Arbeit weder vollständig noch in wesentlichen Teilen bereits veröffentlicht habe sowie dass das in Dateiform eingereichte Exemplar mit eingereichten gebundenen Exemplaren übereinstimmt.

Teile des Kapitels 5 waren mit Rücksprache des Vorsitzenden des Prüfungsausschusses Gegenstand einer Posterpräsentation der DPG-Tagung der Sektion Materie und Kosmos 2021 (SMuK 2021) unter dem Titel "Modelling of plasma ion heat flux in the edge of ASDEX Upgrade with EMC3-EIRENE for an improved understanding of the H-Mode access".

Tübingen, den 01. Dezember 2021

Philipp Sauter

(This page is intentionally left blank)

Contents

1	Motivation to conduct research on separatrix density in nuclear fusion	1
2	Fundamental properties of nuclear fusion and plasma physics	3
2.1	Nuclear Fusion	3
2.2	Tokamak	4
2.3	Divertor Configuration	6
2.4	L-Mode and H-Mode	7
2.5	Confinement factor H_{98}	7
2.6	Diagnostics	8
2.6.1	Thomson Scattering	9
2.6.2	Integrated Data Analysis	9
2.6.3	Interferometry	11
2.6.4	Charge Exchange Recombination Spectroscopy	11
3	Limiting factor one: turbulence at the separatrix	13
3.1	Fundamental concepts of turbulences	13
3.1.1	Fundamental theory of turbulence at separatrix	13
3.1.2	Drift-Wave-Interchange-Turbulence Control Parameter	14
3.2	Influence of edge turbulences on pedestal and core confinement	17
3.2.1	Determining the pedestal	18
3.2.2	Correlation of α_t to electron pedestal top pressure	18
3.2.3	Correlation of α_t to confinement factor H_{98}	26
3.2.4	Influence of $n_{e,sep}$ and $T_{e,sep}$ on pedestal degradation	29
3.2.5	Conclusion on α_t dependence for the given data base	34

4	Limiting factor two: H-Mode density limit	35
4.1	Theoretical description of density limits	35
4.1.1	Greenwald-limit and H-Mode density limit	35
4.1.2	HDL phases	37
4.2	Correlation between phases, separatrix temperature and density	38
5	Limiting factor three: Heat flux in the edge	43
5.1	Theoretical description of heat fluxes	43
5.2	Understanding behaviour via simulations	44
5.2.1	EMC3-EIRENE	44
5.2.2	Discharges	44
5.2.3	Determining heat and diffusion coefficients	47
5.2.4	Heat transport within confinement region	53
5.2.5	Heat transport in the SOL	65
5.2.6	Conclusion on heat flux behaviour in the edge	66
6	Conclusion	67
Appendix A List of discharges used		69
A.1	List of discharges used in chapter 2.6.2	69
A.2	List of discharges used in chapter 3.2	69
A.3	List of discharges used in chapter 4.2	70
Appendix B Additional plots of heat flux analysis in the edge		71
B.1	Determining heat and diffusion coefficients	71
B.2	Heat transport at the separatrix	73
B.3	Separatrix temperature	74
B.4	Decay lengths	75
B.5	Ratios of temperatures and temperature decay lengths	76
B.6	Heat transport in the SOL	77
Bibliography		81

Chapter 1

Motivation to conduct research on separatrix density in nuclear fusion

The vision of nuclear fusion is to provide mankind with an inexhaustible source of renewable environmental-friendly energy. By fusing two atomic nuclei into one, the Universe's most powerful force - the strong nuclear force - can be exploited. In order to achieve this vision, certain aspects of plasma physics need to be understood. One key element is the so called triple-product.

As *Lawson* analyzed in 1955, three main quantities are important in order to achieve a self-burning plasma [1]: Temperature T , particle density n and confinement time τ_E . Nowadays, the so-called triple product is used to define a threshold that has to be exceeded [2]:

$$\bar{n}\bar{T}\tau_E > 3 \times 10^{24} \text{ eVs/m}^3 \quad (1.1)$$

Problematically, those three quantities cannot be increased to an arbitrary level.

Firstly, the confinement time τ_E is characterized by turbulences. Thus, understanding turbulences is crucial in order to build fusion reactors as a potential source of energy, being object of research in chapter 3.

Secondly, the density n is limited by certain density limits. Understanding and exceeding these limits can help to extend the operational space of fusion devices. Therefore,

they are analyzed in chapter 4.

Thirdly, temperatures T are restricted by the input heating of a plasma due to technological reasons. However, temperatures differ at different regions in a fusion device. This distribution is determined by heat fluxes. In order to understand this phenomenon extensively, chapter 5 focuses on heat fluxes.

These parameters are correlated between different regions of the fusion device as they cannot be changed in the core without an influence to the edge. In addition to that, these parameters are co-dependent to each other. In experiments, the density is easily adjustable. Consequently, this thesis focuses on the density and its influence on these parameters.

Chapter 2

Fundamental properties of nuclear fusion and plasma physics

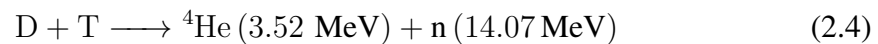
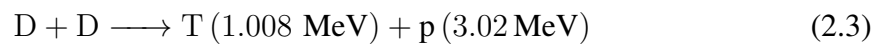
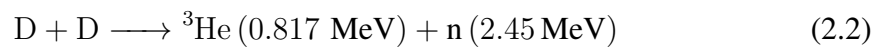
2.1 Nuclear Fusion

In order to nuclear fusion to occur, the Coulomb barrier of the atomic nucleus must be overcome [3]:

$$E_{\text{kin}} \geq \frac{Z_1 Z_2 e^2}{4\pi\epsilon_0(a_1 + a_2)} \quad (2.1)$$

where Z describes the atomic number of the reactant, a its radius, e the elementary charge and ϵ_0 the vacuum permittivity.

In nuclear fusion research, following reactions are considered to be potentially usable by humanity in future fusion reactors [4, p. 255]:



Whereas Deuterium fusion processes are already in use at modern fusion devices such as ASDEX Upgrade, JET or MAST, high energetic fusion reactions containing Tritium have already been tested in JET and are envisaged to take place regularly at ITER from

2035 onwards.

2.2 Tokamak

¹ In order to overcome the Coulomb barrier between two positively charged nuclei, fusion occurs at temperatures of several million degrees centigrade, corresponding to energies of several keV. At these temperatures, matter is in its fourth state - the plasma state. A plasma is an ionized gas. Due to these high temperatures, no material can sustain direct contact. In the Sun and in every other star, plasma is confined due to gravitational pressure. It is obvious, that gravitational confinement is not an option on Earth. Nevertheless, we can use the properties of plasma being an ionized gas. Due to the Lorentz force, a charged particle is bound to magnetic field lines [6]. As a consequence, by applying external magnetic fields, plasma can be magnetically confined. Within the last decades, two different kinds of fusion devices confining plasma magnetically were developed. On the one hand, there is the concept of a stellarator, a fusion device with a complex geometry; on the other hand, the concept of a tokamak with a torus shaped geometry. The experiments at Max-Planck-Institut für Plasmaphysik at Garching uses the tokamak ASDEX Upgrade and the soon biggest experiment in the field of nuclear fusion, ITER, will be a tokamak as well. This work will focus on a tokamak configuration.

As shown in Fig. 2.1, a tokamak consists of a torus-shaped plasma vessel. In order to confine plasma magnetically, three set of magnetic coils are used. Primarily, a toroidal magnetic field B_{tor} is produced by outer poloidal field coils (blue). As it is visible in Fig. 2.1, the different coils are closer together on the inside of the torus (so called high-field side HFS) than on the outside (so called low-field side LFS). Therefore, the magnetic field is higher close to the center than at outer parts. This leads to a gradient in the field, $\nabla \cdot \mathbf{B}$, inducing a drift [8, p. 4]:

$$v_{\nabla B} = \frac{E_{kin,\perp}}{q} \frac{B \times \nabla B}{B^3} \quad (2.5)$$

¹This section is adapted from this author's previous Bachelor thesis [5].

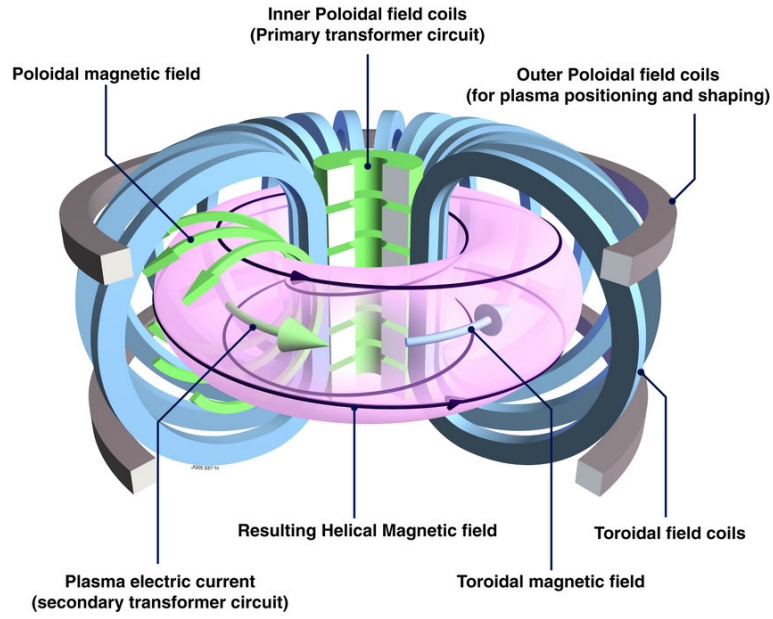


Figure 2.1: Schematic view of a tokamak, [7].

Where $E_{\text{kin},\perp}$ is the perpendicular kinetic energy of a particle, and q its magnetic charge. Since the direction of $v_{\nabla B}$ is dependent on the sign of the charge, positive and negative charges will be separated, which produces an electric field \mathbf{E} . In turn, this electric field produces another drift [8, p. 4]:

$$v_{\mathbf{E}} = \frac{\mathbf{E} \times \mathbf{B}}{B^2} \quad (2.6)$$

That drift - affecting both electrons and ions in the same way - leads to a movement of the plasma towards the wall which can only be averted if the electric field and thus charge separation are avoided. This is done by a poloidal magnetic field B_{pol} , produced by the inner poloidal field coils (green), which together with the plasma current acts as a transformer.

The superposition of both of these fields, B_{tor} and B_{pol} , leads to helically wound magnetic field lines.

Lastly, a pair of Helmholtz coils (outer poloidal field coils, gray) produces a homogeneous magnetic field B_z preventing the plasma from expanding outwards in a horizontal

direction.

2.3 Divertor Configuration

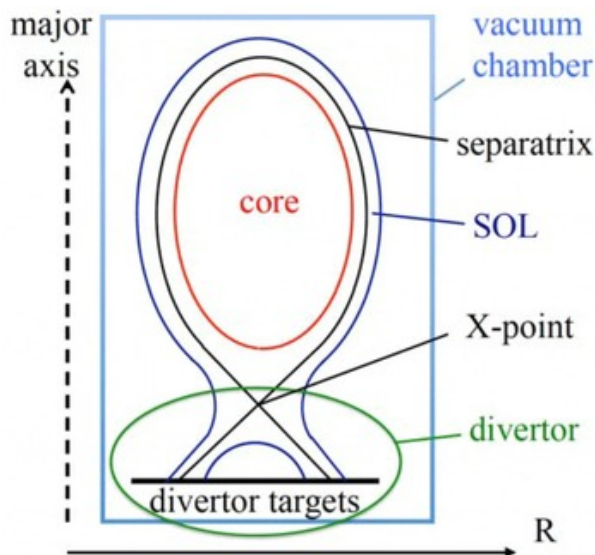


Figure 2.2: Schematic draw of a divertor configuration, [9].

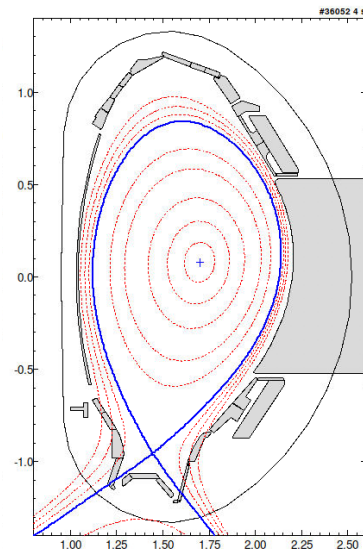


Figure 2.3: Plasma analysis in ASDEX Upgrade.

² In theory, the magnetic field lines are parallel to the wall. However, since the wall consists of discrete plates, it is impossible to achieve perfect parallelism. Thus, field lines can intersect with the wall and transport matter to it [4, p. 139]. With the purpose of controlling this unavoidable interaction, a divertor configuration is used. By using a divertor, the wall-plasma interaction is dislodged from the core. While this leads to preventing the core plasma from impurities, it also reduces the temperature of the interacting plasma.

In a divertor configuration, the confined area, i.e. the area where magnetic field lines are closed, is limited by the so-called separatrix. The separatrix crosses itself in the so-called X-point and separates the confined area from the so-called scrape-off-layer

²This section is adapted from this author's previous Bachelor thesis [5].

(SOL). Charged particles in the SOL follow magnetic fields line and eventually collide with the divertor plates. The point where the separatrix crosses the divertor target is called strike point. Finally, the area of the SOL between target and X-point is called divertor leg. Figure 2.2 shows a schematic draw of a divertor configuration in a poloidal profile. One can differentiate between two divertors, first an inner divertor, meaning the divertor which is closer to the center of torus, i.e. the high-field side, and second an outer divertor at the low-field side.

Figure 2.3 demonstrates an interpolation of the magnetic field of a discharge in ASDEX Upgrade. While the blue lines marks the separatrix, red lines mark flux surfaces.

2.4 L-Mode and H-Mode

In a tokamak, mainly two dissimilar modes can be distinguished, differing by its degree of confinement: L-Mode (L for low confinement) and H-Mode (H for high confinement) [10]. When initiating a plasma, it starts at L-Mode. Once it is heated above a certain threshold, the plasma enters an H-Mode [11]. Due to its benefits, it is envisaged to operate ITER as well as possible future fusion reactors in such H-Modes. This high degree of confinement is achieved by a pedestal in pressure which forms near the separatrix.

As evident in Fig. 2.4, the pressure gradient possesses a sharp bend. The area in which the pressure gradient decreases rapidly is known as the so-called pedestal region. The reference with a pedestal becomes clear when one takes a look at Fig. 2.4. This pedestal is characterized by a certain pressure, the so-called pedestal pressure. One should keep in mind, that this pressure is composed by an electron pedestal pressure p_e and an ion pedestal pressure p_i . Lastly, the pedestal pressure at the edge of the plasma is called top pedestal pressure. It can be found at a flux surface of about $\rho_{\text{pol}} = 0.95$, meaning that 95 % of the plasma current lies within this flux surface.

2.5 Confinement factor H_{98}

The quality of confinement of an H-Mode plasma is characterized by the confinement factor H_{98} , introduced by [13]. This factor compares the energy confinement time τ_E with the energy confinement time obtained by a multi-machine scaling of H-Modes

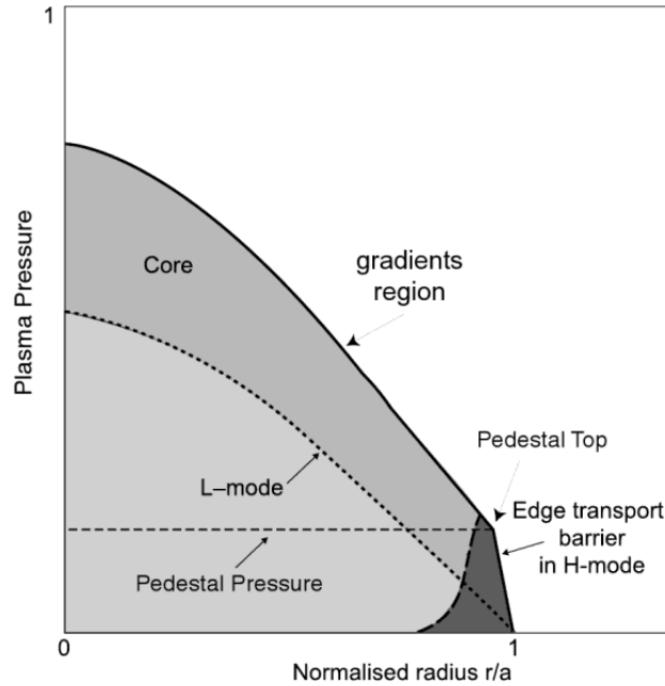


Figure 2.4: Pressure radial profile structure in an H-Mode [12, p. 64].

done by the ITER Physics Expert Group in 1998 [13], called $IPB(y,2)$. The closer the values are to one, the better the H-Mode confinement is. Even though this value was originally introduced to describe H-Modes, this factor is simultaneously calculated for L-Modes, leading to values in the range of about 0.6 [14].

This confinement factor is also determined by the pedestal and the plasma triangularity δ . The triangularity is the result of the plasma not being perfectly elliptical as seen in Fig. 2.6 and represents the horizontal distance between the plasma major radius and the X-Point. The higher δ , the higher the pedestal is. If the pedestal enlarges, the confinement in the core improves, leading to an increase in H_{98} .

2.6 Diagnostics

For this thesis, mainly four of ASDEX Upgrade's diagnostics are used.

2.6.1 Thomson Scattering

In this context, Thomson scattering is the most efficient approach to measure temperatures and densities of electrons at the separatrix. Thomson scattering describes the elastic scattering of an incident electromagnetic wave by a free particle [17]. The free particle, mostly electrons since $m_e \ll m_i$, is accelerated by the incident wave. The acceleration of the particle leads to an accelerated charge, which by itself emits radiation with the same frequency as the incident wave [18]. The intensity of the scattered wave depends on the electron density. Additionally, due to the Doppler effect, the scattered radiation is shifted. By fitting a Maxwellian distribution function to this shift, the velocity of the scattering electron can be calculated and thus its temperature. ASDEX Upgrade is equipped with two Thomson Scattering arrays, containing four (core) and six (edge) lasers. In this analysis, the edge Thomson array is mainly used. As Fig. 2.5 indicates, this array is limited to a small range in the edge, covering a range of about 10 to 15 mm. Therefore, this method is used to measure electron density and temperature in the vicinity of the separatrix.

Due to the shape of the plasma on the outer edge, each laser has its unique Z and R value. To get a continuous profile of electron density and temperature, these measurements have to be mapped to a common flux surface. In this analysis due to the poloidal symmetry, data is mapped to the outer midplane.

2.6.2 Integrated Data Analysis

Another possibility to obtain electron temperature and density profiles lies in the usage of integrated data analysis (IDA), presented in [19]. This complex code combines different diagnostics of ASDEX Upgrade such as for example laser interferometry, Lithium beam emission spectroscopy and Thomson scattering. The IDA code reconstructs profiles by using Bayesian probability theory. Although IDA data is convenient for analysis in the core or at the pedestal, it is inaccurate for the separatrix.

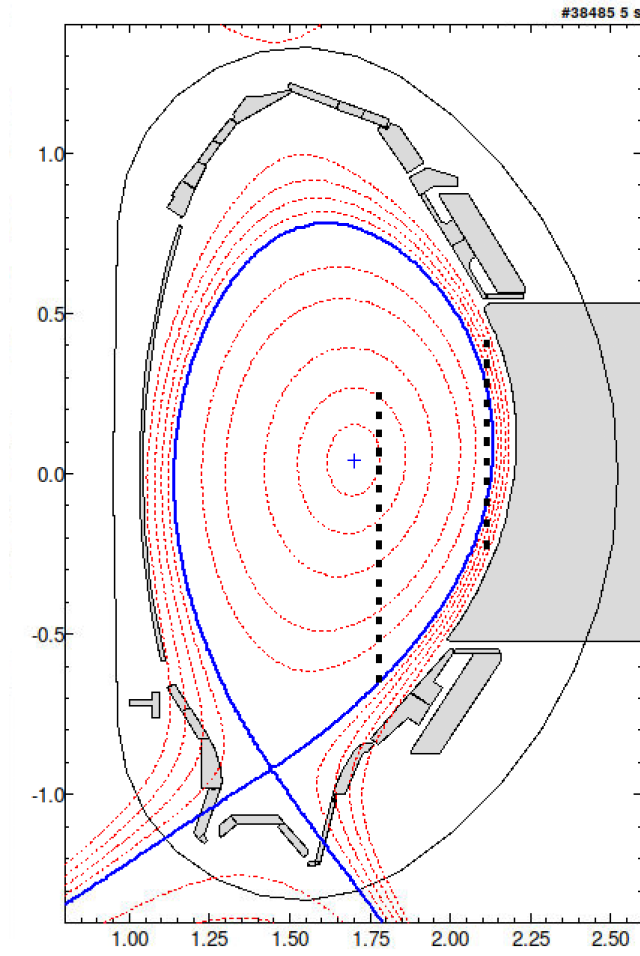
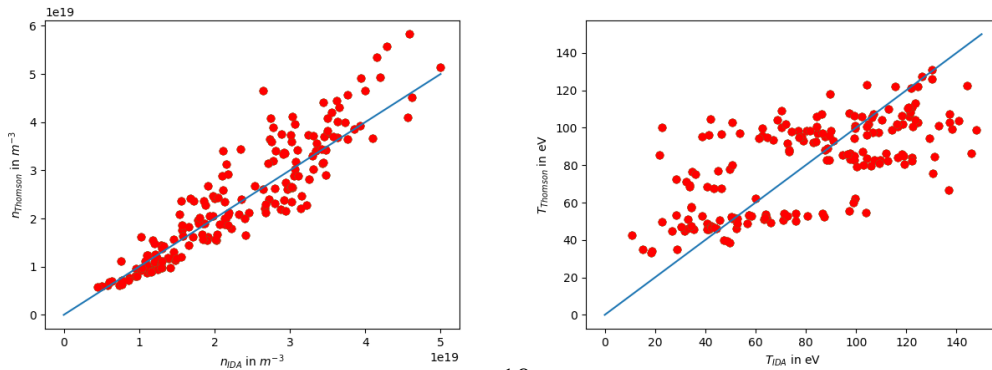


Figure 2.5: Poloidal cross-section of discharge of 38485 at 5.0 s. The x-axis depicts the poloidal radius R in m, the y-axis represents the vertical distance to the midplane Z in m. The vertical dashed black lines represent the light path of ASDEX Upgrade's two Thomson Scattering diagnostics.



10

Figure 2.6: Comparison of electron density (left) and electron temperature (right) at the separatrix obtained by Thomson scattering and IDA. For discharges used, c.f. appendix A.1

Fig. 2.6 shows that significant deviations exist between IDA and Thomson scattering, especially for electron temperatures at the edge. Thus, IDA data in this thesis is only used for core and pedestal values as well as for densities.

2.6.3 Interferometry

ASDEX Upgrade is also equipped with deuterium cyanide (DCN) lasers [20]. The plasma has a different refractive index than the vacuum within the vessel. This refractive index depends on the electron density. By measuring the phase difference in an interferometer between the laser traversing the plasma and the laser traversing a vacuum, the refractive index can be calculated. Once the refractive index is calculated, a line-integrated density of the laser path can be determined. Fig. 2.7 depicts ASDEX Upgrade's H-5 laser describes the line-integrated density at the edge while data from the H-1 laser corresponds to the line-integrated density at the core.

2.6.4 Charge Exchange Recombination Spectroscopy

Charge exchange recombination spectroscopy (CXRS) measures the radiation spectrum caused by the excitation of impurities by a charge exchange reaction with fast neutral atoms [21]. From this spectrum, ion temperatures can be derived. At the edge, this diagnostic is called CMZ.

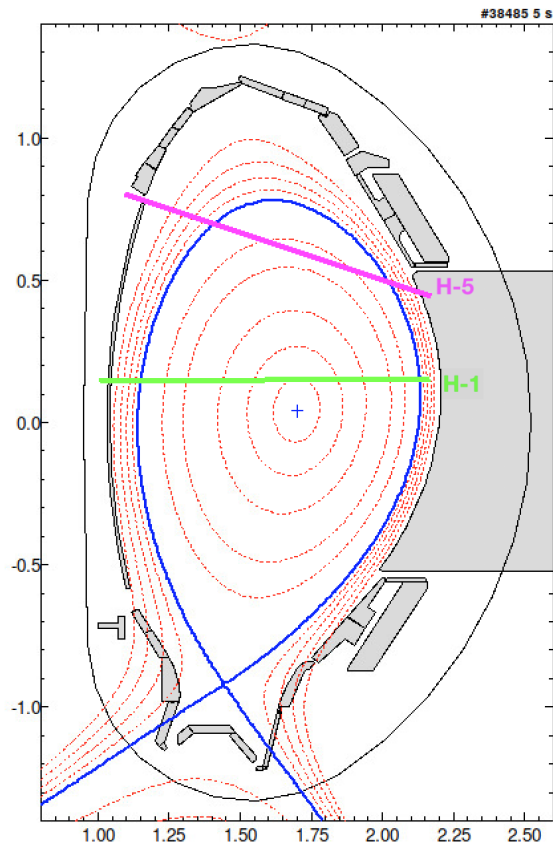


Figure 2.7: Poloidal cross-section of discharge of 38485 at 5.0 s. The x-axis depicts the poloidal radius R in m, the y-axis represents the vertical distance to the midplane Z in m. The pink lines represents laser H-5, the green line depicts laser H-1.

Chapter 3

Limiting factor one: turbulence at the separatrix

3.1 Fundamental concepts of turbulences

3.1.1 Fundamental theory of turbulence at separatrix

Turbulences in plasmas are categorized into drift wave turbulences and interchange turbulences.

Drift wave turbulences

As mentioned before, both ions and electrons experience electro-magnetic drifts.

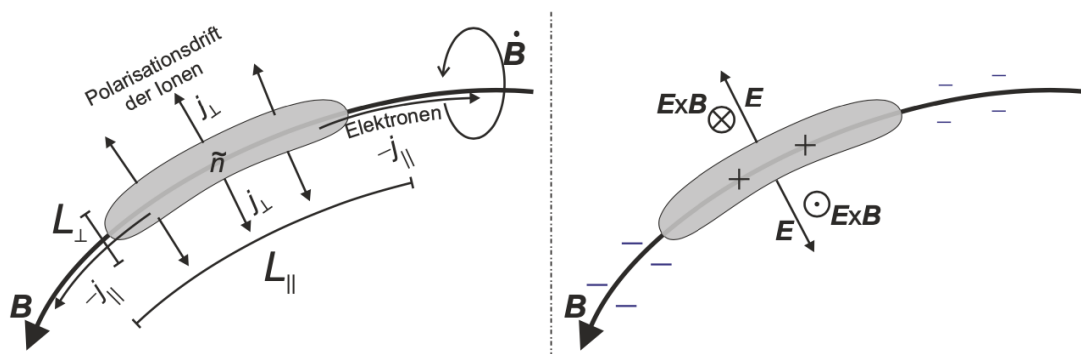


Figure 3.1: Three dimensional dynamics of drift waves. A density perturbation (left) induces a current, leading to charges, electric fields and drifts (right). Adapted from [2].

Assume a positive density perturbation \tilde{n} , which is elongated in the direction of a magnetic field line, $L_{\parallel} \gg L_{\perp}$. Since the ion density is increased along the field line, a pressure gradient is induced in parallel direction. Electrons react to that gradient and are pushed outwards, leading to a negative parallel current $-j_{\parallel}$. As a consequence, charges are separated to a certain extent, resulting in a positive potential at the volume of the density perturbation \tilde{n} . One must keep in mind that this density perturbation is strongly limited and is primarily elongated in parallel direction to the field line. The density in the background plasma remains constant at first. Nevertheless, the background plasma will eventually react to this perturbation and induces an $E \times B$ drift, leading to a vortex in a cross-sectional view.

Three processes are essential for drift waves: First, they are three dimensional. Second, electrons dominate the parallel dynamic. Third, ions dominate the perpendicular dynamic [2].

Interchange instability

Interchange instabilities are caused by a steep gradient in the magnetic pressure of a confined plasma [22], regularly in areas where the magnetic field lines are curved. During this state of stability, the plasma can change places with magnetic fields, since this interchange is energetically favorable [23].

Fig. 3.2 shows that at the boundary interface between two different mass densities local space-charge regions are created, which repeat themselves periodically with a change of its charge. These space-charge regions induce another electric field, which is anti-parallel to the diamagnetic drift, causing a destabilization of the plasma.

3.1.2 Drift-Wave-Interchange-Turbulence Control Parameter

Turbulences are difficult to describe analytically. To simplify, *Scott* analyzed the impact of interchange effects on drift wave turbulences, [24] [25].

The strength of interchange turbulences is characterized by a frequency

$$\omega_B = \frac{2\lambda_p}{R} \left(1 + \frac{1}{Z} \right). \quad (3.1)$$

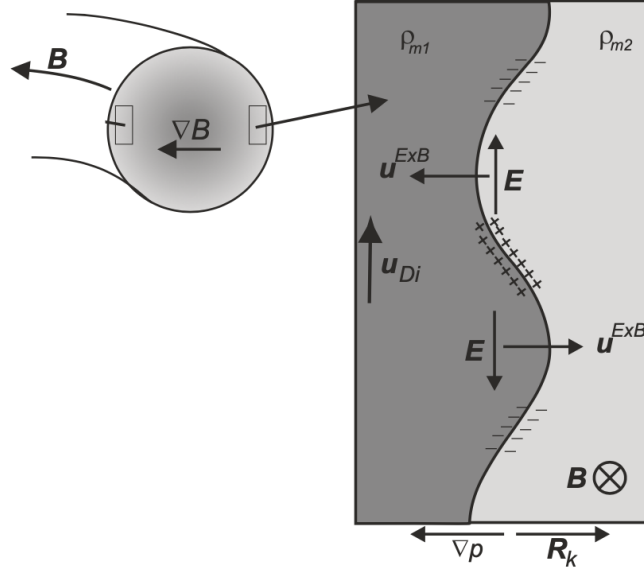


Figure 3.2: Depiction of the influence of curved magnetic field lines on the outer side of a toroidal plasma, adapted from [2]. \mathbf{u}_{Di} represents the diamagnetic drift in the plasma, $\mathbf{u}^{E \times B}$ is the drift introduced in Eqn. (2.6), \mathbf{E} represents the electric and \mathbf{B} the magnetic field. ρ_m is the mass density, here: $\rho_{m1} > \rho_{m2}$. ∇p depicts the pressure gradient, \mathbf{R}_k is the poloidal radius.

R denotes the major radius of the machine, λ_p the plasma pressure gradient scale length and $\bar{Z} = n_e / (\sum_j n_j)$ the average ion charge, which depends on the electron density n_e and on individual densities n_j of j different ion species.

On the other hand, a normalized collisionality C can be derived [16]:

$$C = 0.51 \nu_{ei} \frac{\lambda_p}{c_s} \left(\frac{m_e}{M_i} \right) \left(\frac{\hat{q}_{cyl} R}{\lambda_p} \right)^2 \quad (3.2)$$

c_s denotes the speed of sound, m_e the mass of an electron, R the major radius of the machine and \hat{q}_{cyl} the cyclical safety factor. M_i is a characteristic ion mass with the assumption of quasi-neutrality:

$$M_i = \frac{\sum_j n_j M_j}{n_e} \quad (3.3)$$

ν_{ei} is the electron-ion Braginskii collision frequency [26]:

$$\nu_{ei} \approx \nu_{ee} = \frac{4\sqrt{\pi}}{3} \frac{n_e e^4 \ln \Lambda}{(4\pi\epsilon_0)^2 \sqrt{m_e} T_e^{3/2}}, \quad (3.4)$$

which depends on the elementary charge e , vacuum permittivity ϵ_0 , electron mass m_e and the Coulomb logarithm $\ln \Lambda$. A normalized collisionality C can be derived:

$$C = 0.51 \nu_{ei} \frac{\lambda_p}{c_s} \left(\frac{m_e}{M_i} \right) \left(\frac{\hat{q}_{\text{cyl}} R}{\lambda_p} \right)^2 \quad (3.5)$$

In order to get a turbulence parameter independent of λ_p - a parameter which is useful for regression studies with decay lengths -, *Eich et al* propose a turbulence parameter [16]:

$$\alpha_t := C \omega_B = 1.02 \frac{\nu_{ei}}{c_s} \frac{m_e}{M_i} \hat{q}_{\text{cyl}}^2 R \cdot \left(1 + \frac{1}{Z} \right) \quad (3.6)$$

Assuming a low concentration of impurities - which is an appropriate approximation for many discharges -, estimating the Coulomb logarithm $\ln \Lambda \approx 13.7$ and using mean values $T_{\text{sep}} = 91$ eV as well as $n_{\text{sep}} = 2.5 \cdot 10^{19} \text{ m}^{-3}$, (3.6) can be reduced to [16]:

$$\alpha_t \approx 3 \cdot 10^{-18} \hat{q}_{\text{cyl}}^2 R \frac{n_e}{T_e^2} Z_{\text{eff}} \quad (3.7)$$

Thus, α_t is linearly dependent on n_e and inversely quadratic dependent on T_e . It must be underlined that these are values taken at the separatrix and that these parameters are correlated by the pressure $p = nT$.

With α_t , the transition from drift wave to interchange turbulences can be described. When $\alpha_t < 1$, instabilities are mainly driven by interchange turbulences. Once $\alpha_t > 1$, transport is dominated by drift wave turbulences.

3.2 Influence of edge turbulences on pedestal and core confinement

Recent activities introduced the parameter α_t [16]. On the one hand, they revealed correlations between edge turbulences and decay length widths at the separatrix. On the other hand, an influence of edge turbulences on the core confinement parameter H_{98} was indicated. In addition to that, this study could not find H-Mode discharges with values of $\alpha_t > 1$. This hints to a correlation between this turbulence control parameter and the L-Mode/H-Mode transition threshold.

This work was later extended [27] to the correlation between α_t and different plasma regimes. A correlation between confinement and α_t is indicated as seen in Fig. 3.3.

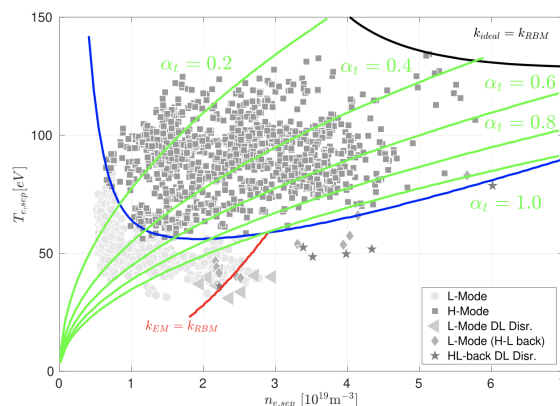


Figure 3.3: Separatrix operational space, adapted from [27]. The blue line indicates the L-Mode/H-Mode threshold, green lines show α_t isobars. The black line corresponds to another limit, the to so called ballooning instabilities. Data points are from a data base similar to A.2.

α_t is understood as a turbulence control parameter between drift wave and interchange instabilities at the separatrix. However, the correlation between α_t and pedestal quantities has not been yet object of research. In addition to that, the correlation between α_t and core confinement remains unclear. The aim of this chapter is to analyse these correlations.

3.2.1 Determining the pedestal

Before correlating α_t to the pedestal, it is essential to define its exact position. Usually, the pedestal is assumed to be at $\rho = 0.96$. However, the accurate position of the pedestal can be determined with the two line method described by [28]. The pedestal top is characterised by a sharp dip - a turning point - in plasma pressure. Near this turning point, the pressure can be approximated by two different linear functions:

$$p(\rho) = \begin{cases} a_2(a_0 - \rho) + a_1 & \text{for } \rho \leq a_0 \\ a_3(\rho - a_0) + a_1 & \text{for } \rho > a_0 \end{cases} \quad (3.8)$$

a_2 and a_3 describe the slope of the linear functions, a_1 the y intercept and a_0 the breaking-point, corresponding to the position of the pedestal top.

This method is applied to a data base consisting of about 200 discharges by calculating the parameters with the code described in [29]. For the most part of this data base, the pedestal can be found in an interval of $\rho = 0.96 \pm 0.01$. However, this method is of restricted validity in areas of a flat pedestal. Due to this flatness, the determination of the breaking point a_0 becomes vague since a small change in slope leads to a significant shift in the breaking point.

However, the two line method validated a pedestal top position of about $\rho = 0.96$ at steeper pedestals. For further analysis, this value will be used with $\rho = 0.95$ as lower and $\rho = 0.97$ as upper limit.

3.2.2 Correlation of α_t to electron pedestal top pressure

α_t is a turbulence parameter measured at the separatrix, corresponding to $\rho = 1$, while the pedestal top can be found near $\rho = 0.96$. For this analysis, a data base consisting of 114 discharges from ASDEX Upgrade was used. The data base used in this chapter can be found in A.2.

In order to compare α_t with the electron pedestal top pressure, α_t is computed by using Thomson data of n_e and T_e . Z_{eff} is fixed at a value of 1.25. The toroidal magnetic field remains almost constant at $B_{\text{tor}} = 2.5$ T and the plasma current is in the range of 800 kA. Additionally, $p_{e,\text{top}}$ is taken from the IDA data base at $\rho = 0.96$ with an errorbar of values at $\rho = 0.95$ and $\rho = 0.97$.

Fig. 3.4 shows a correlation between α_t and pedestal top pressure. While higher pedestal top pressures dominate at lower α_t , higher values of α_t lead to lower pressures. Notably, a triangle is created for pressures higher than approximately 2000 Pa. Below that pressure, $p_{e,top}$ remains constant for all α_t .

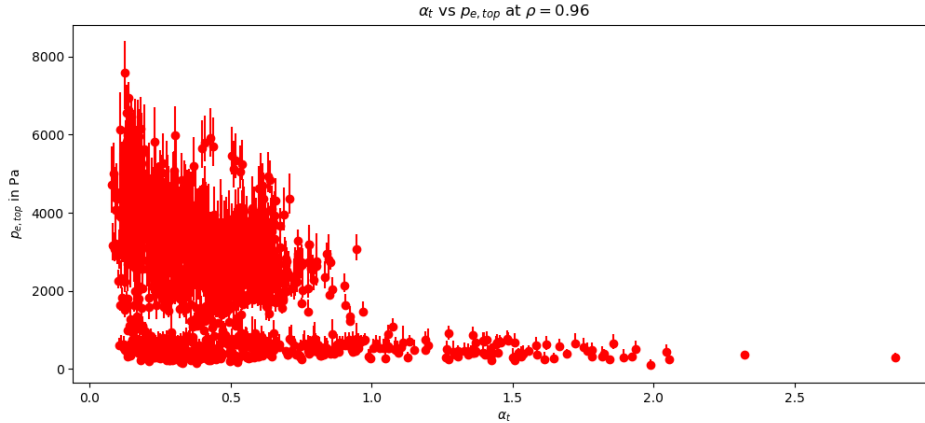


Figure 3.4: Comparison of α_t with p_e at $\rho = 0.96 \pm 0.01$.

To understand this cloud better, individual data points are color coded with their respective mode. Here, five operational modes are distinguished:

1. Mode 1 - L-Mode: In this phase, the plasma is in a stable L-Mode after heating of the plasma has started.
2. Mode 2 - H-Mode: In this phase, the plasma is in a stable H-Mode. In order to get to an H-Mode, the power within the plasma must be increased to overcome a characteristic threshold. This is done by further heating.
3. Mode 3 - L-Mode density limit (LDL): Instead of continuing to heat an L-Mode, its density can be increased. By doing so, the plasma can be driven to its density limit. Once it reaches the L-Mode density limit, the plasma disrupts.
4. Mode 4 - L-Mode after H-L back transition (LHL back transition): Once an H-Mode reaches a certain density limit, it turns back into an L-Mode (cf. section 4.1.1). In order to differentiate this L-Mode from an initial L-Mode (mode 1),

a distinguished mode is assigned to this L-Mode. This differentiation might be convenient to detect hysteresis effects.

5. Mode 5 - HL-back transition density limit (LHL DL disruption): A plasma in an L-Mode after its back transition from H-Mode can reach an L-Mode density limit as well. Thus, it is mode 3 after an L-H back transition.

Nevertheless, it must be noted that not all phases can be found in each individual discharge. Some discharges were specifically made to reach the H-Mode density limit. However, a subset of discharges disrupted before reaching that limit.

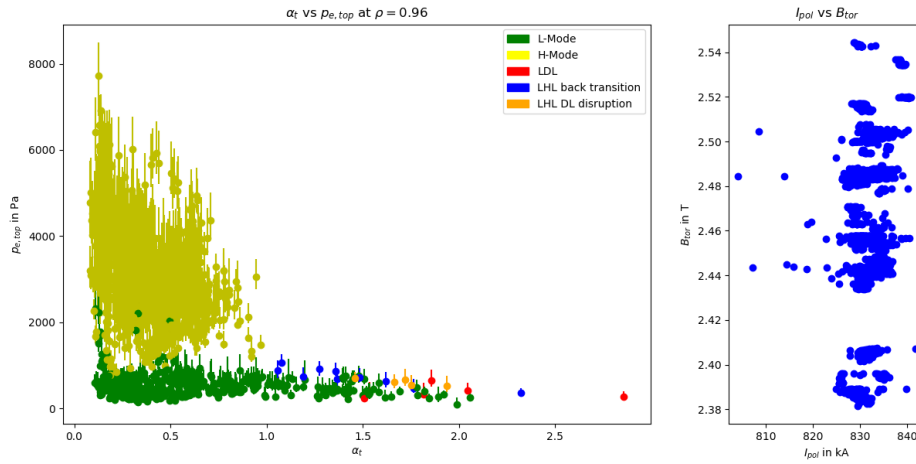


Figure 3.5: Left: Comparison of α_t with p_e at $\rho = 0.96 \pm 0.01$ with phases. Right: Distribution of I_{pol} and B_{tor} .

Fig. 3.5 shows a clear difference between L-Mode and H-Mode. Some L-Mode data points can be found within the triangular H-Mode cloud. This is explained by an uncertainty in the determination of a change in mode [30].

Another observation is that no H-Mode data points are found for $\alpha_t > 1$. This is in accordance with findings indicating that the L-H-threshold is correlated with $\alpha_t = 1$, cf. Fig. 3.6.

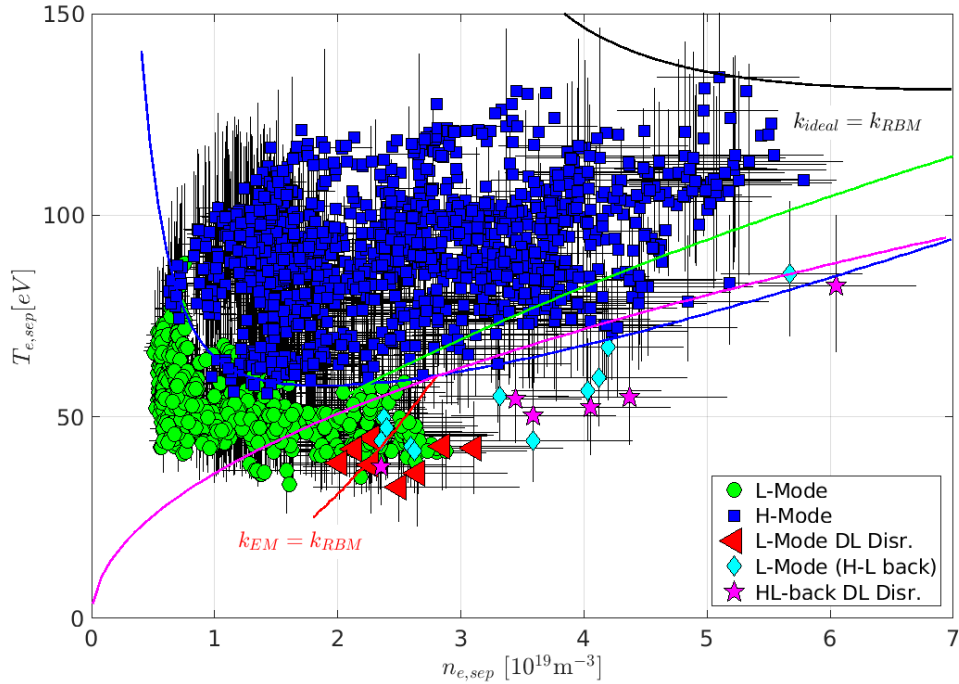


Figure 3.6: Correlation of $T_{e,sep}$ and $n_{e,sep}$ for the same data base. The blue line indicates the threshold between L- and H-Mode, while the magenta line corresponds to $\alpha_t = 1$, adapted after [27].

One explanation for the triangle formed by the H-Mode in Fig. 3.6 could be continued heating. Once plasma reaches the H-Mode, external heating does not necessarily cease. Continuation of heating leads to an increase in plasma temperature. An increase in plasma temperature generates an increase in pressure ($p = nT$) and a decrease of α_t ($\alpha_t \sim T^{-2}$). However, if the temperature at the pedestal top is extended, the temperature at the separatrix does not increase instantly. Consequently, if H-Mode data points are limited to points in time once the maximum stored energy in the plasma is reached, fewer data points for low α_t and $p_{e,top}$ are expected. This filtering method in Fig. 3.7 confirms that the lower left part of the triangle is induced by ongoing heating. Filtered data now suggest that α_t has an exponentially decaying correlation with $p_{e,top}$.

Filtered data is now object of regression studies in order to find the correlating physical quantities which lead to the degradation. A first approach is to regress a simple

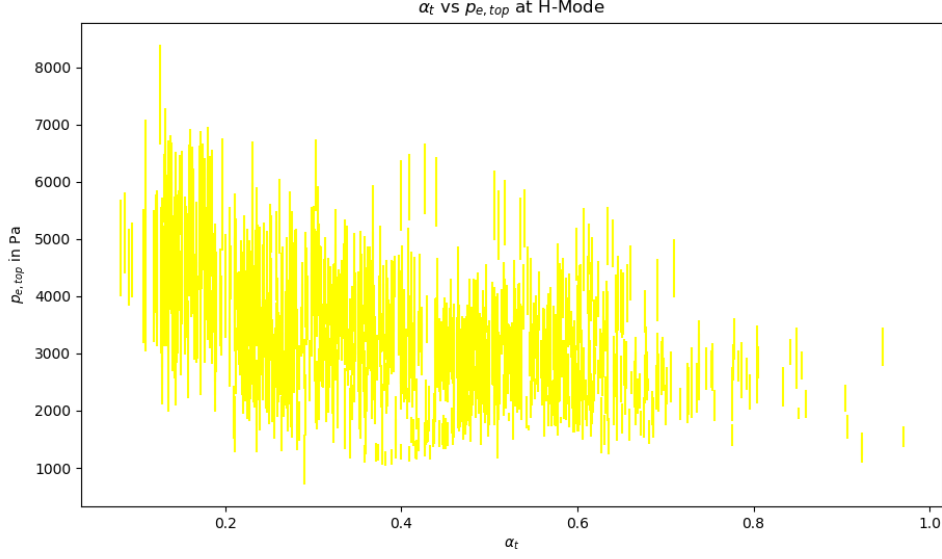


Figure 3.7: Comparison of α_t with $p_{e,top}$ for H-Mode after having reached the maximum store plasma energy.

power law:

$$p_{e,top} = a \cdot \alpha_t^b \quad (3.9)$$

This regression (Fig. 3.8) shows a relative root mean square error (RMSE) of 26.0%. It implicates a correlation $p_{e,top} \sim \alpha_t^{-1/3}$. Since $\alpha_t \sim \frac{n_{e,sep}}{T_{e,sep}^2}$, this leads to $p_{e,top} \sim \frac{T_{e,sep}^{2/3}}{n_{e,sep}^{1/3}}$.

However, even though α_t combines different characteristic plasma parameters, a plasma depends on more quantities. One physical property which is of interest is δ , the triangularity, which represents the shape of the plasma. Additionally, the power transported via the separatrix into the scrape-off-layer P_{sol} has a potential influence. It is calculated by the difference of the total heating power and radiation power loss. By considering these quantities in Fig. 3.9, the regression quality represented by the relative root mean square error improves significantly. While the influence of P_{sol} is limited, $p_{e,top}$ shows a strong correlation to the triangularity δ .

Instead of using α_t , recent activities focused on stability physics and used $n_{e,sep}$ nor-

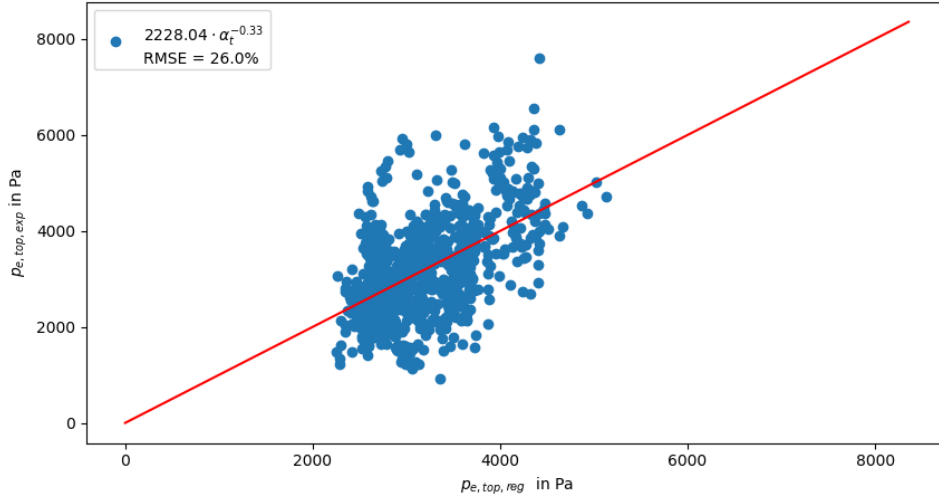


Figure 3.8: Simple exponential regression of $p_{e,top}$ with α_t .

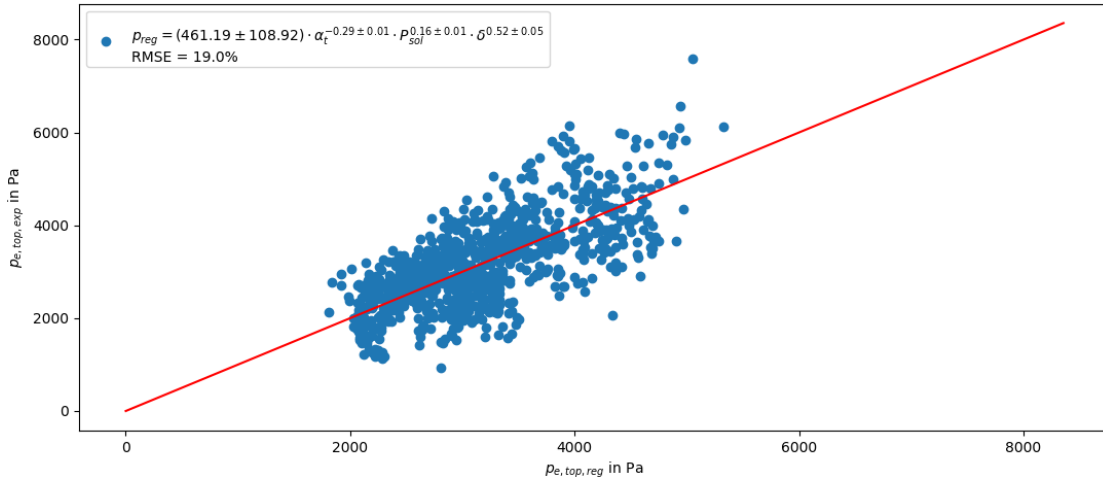


Figure 3.9: Exponential regression of $p_{e,top}$ with α_t taking into account P_{sol} and δ .

malized to $n_{e,top}$ to characterize a correlation between the pedestal and the separatrix [31]. However, one needs to keep a caveat in mind: since $p_{e,top} = n_{e,top}T_{e,top}$, this normalization corresponds to a correlation of $n_{e,top}^2 T_{e,top}$ rather than $p_{e,top}$. Nonetheless, that proposed regression is compared with an α_t regression in Fig. 3.10. The quality of the regression improves slightly. Nevertheless, the influence of δ has changed. One explanation might be that δ has a growing influence on the pedestal stability. Consequently,

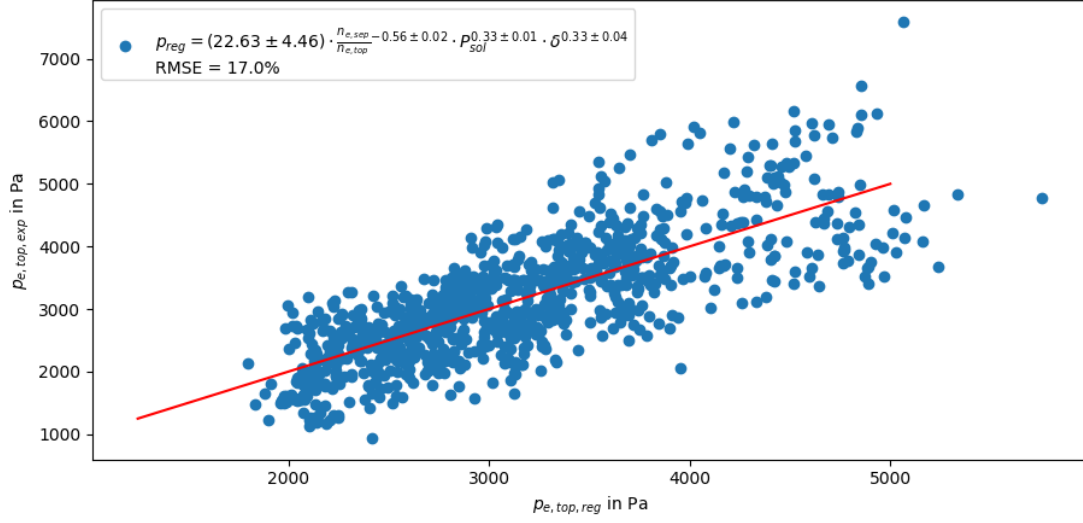


Figure 3.10: Exponential regression of $p_{e,top}$ with $\frac{n_{e,sep}}{n_{e,top}}$ taking into account P_{sol} and δ .

it is concluded that $\frac{n_{e,sep}}{n_{e,top}}$ is similarly suited to characterize the pedestal degradation as α_t . However, the approach not to use α_t as a regression parameter but $n_{e,sep}$ and $T_{e,sep}$ separately can demonstrate the meaningfulness of an α_t regression. It must be noted that a regression combining $T_{e,sep}$ and P_{sol} is not reasonable since these quantities are co-dependent.

For further refinement of regression studies, the subsequent step is to replace α_t by its constituencies $n_{e,sep}$ and $T_{e,sep}$ (Fig. 3.11). The first observation is that this regression has almost the same quality as the regression depicted in Fig. 3.9. Secondly, the correlation with the triangularity has changed from $\delta^{1/2}$ to $\delta^{1/4}$. In order to compare the product of $n_{e,sep}T_{e,sep}$ with their respective exponents, some transformations must be carried out:

$$n_{e,sep}^{-0.27 \pm 0.02} T_{e,sep}^{1.24 \pm 0.06} \approx n_{e,sep}^{1/4} T_{e,sep}^{5/4}. \quad (3.10)$$

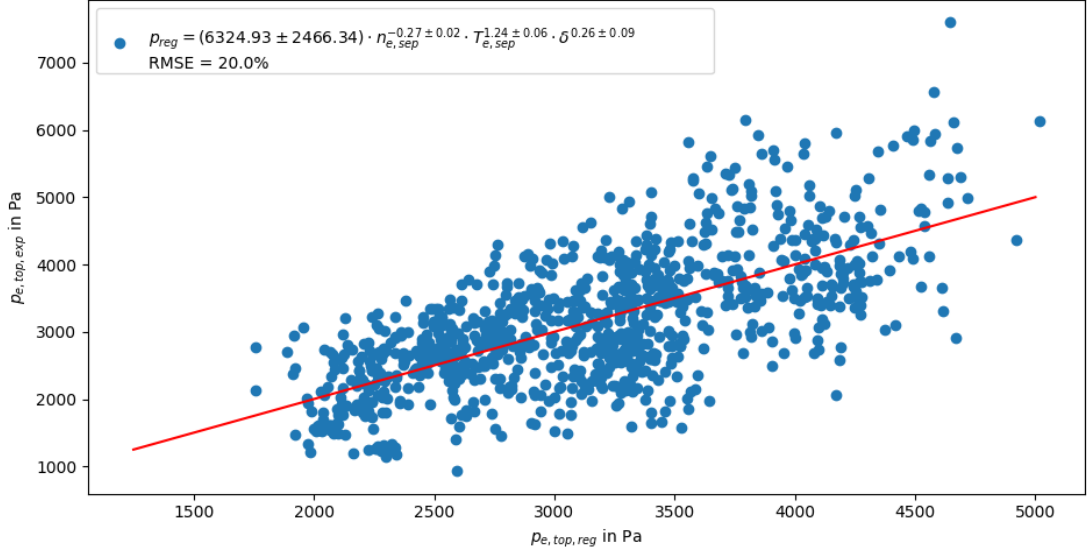


Figure 3.11: Exponential regression of $p_{e,top}$ with $n_{e,sep}$ and $T_{e,sep}$ taking into account δ .

With $p_{e,top} \sim \alpha_t^{-1/3}$ as an approximation from regression 3.9:

$$p_{e,top} \sim \alpha_t^{-1/3} \quad (3.11)$$

$$\sim \left(\frac{n}{T^2} \right)^{1/3} \quad (3.12)$$

$$\sim n_{e,sep}^{1/3} T_{e,sep}^{-2/3} \quad (3.13)$$

$$\not\sim n_{e,sep}^{-1/4} T_{e,sep}^{5/4} \quad (3.14)$$

Ideally, the exponents of Eqns. (3.13) and (3.14) should be identical. However, the exponents differ significantly. As a consequence, the meaningfulness of these regressions is limited. The degradation of the pedestal caused by α_t is therefore not described by a simple deviation in $n_{e,sep}$ or $T_{e,sep}$.

In conclusion, a correlation between α_t and the pedestal degradation cannot be generalized for the given data base.

3.2.3 Correlation of α_t to confinement factor H_{98}

This section extends the study to the correlation between α_t and the core confinement factor H_{98} .

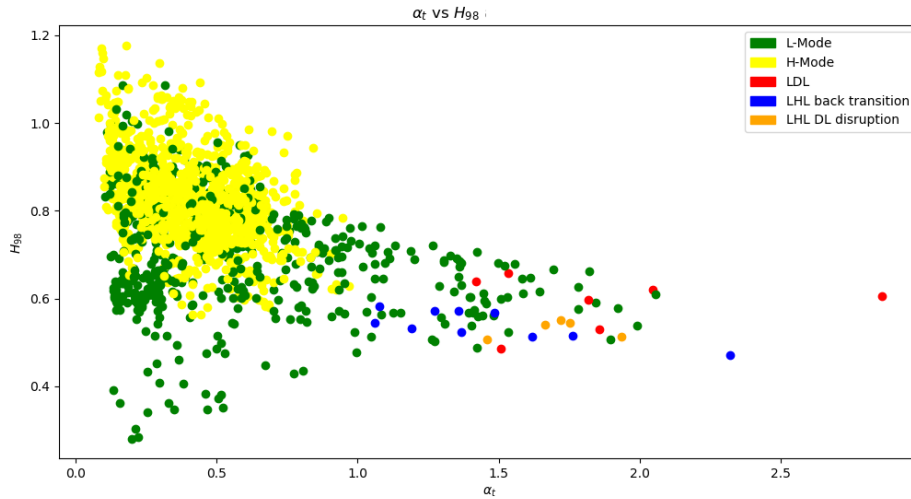


Figure 3.12: Comparison of α_t with $H_{98,y2}$.

Unlike the previous plots, Fig. 3.12 shows no clear differentiation between the phases. A triangle is formed as well but no differentiation between phases is apparent. While L-Mode is constant at low pedestal top pressures with no influence of α_t , L-Modes exist for both low and high H_{98} values. Fig. 3.13 correlates pedestal top electron density to α_t and H_{98} . No clear picture arises. There is only a vague trend that low densities lead to high values of H_{98} .

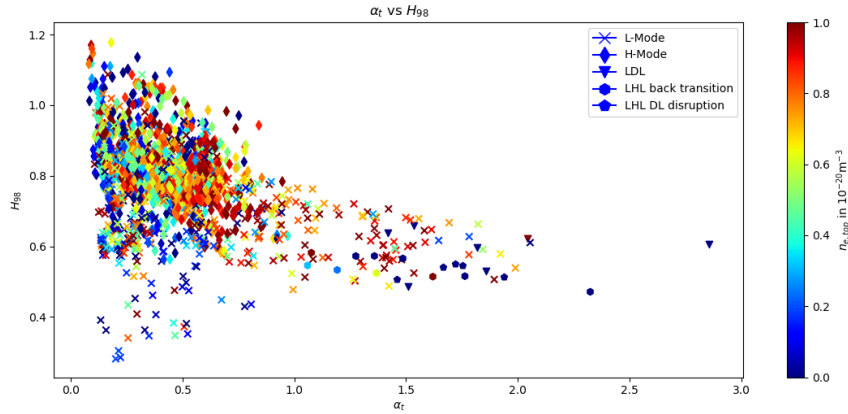


Figure 3.13: Comparison of α_t with $H_{98,y2}$ and $n_{e,top}$.

To continue, a correlation between H_{98} and α_t is sought to be determined via a regression. Firstly, the regression is again limited to H-Mode values after having reached a maximum in plasma stored energy W_{MHD} . A certain degradation can be observed in Fig. 3.14. There are no high values for H_{98} close to or above 1.0 for values of α_t greater than 0.6. Additionally, almost no H_{98} values below 0.7 can be found for $\alpha_t < 0.5$, revealing that the confinement of the plasma worsens with an increase of interchange instability turbulences.

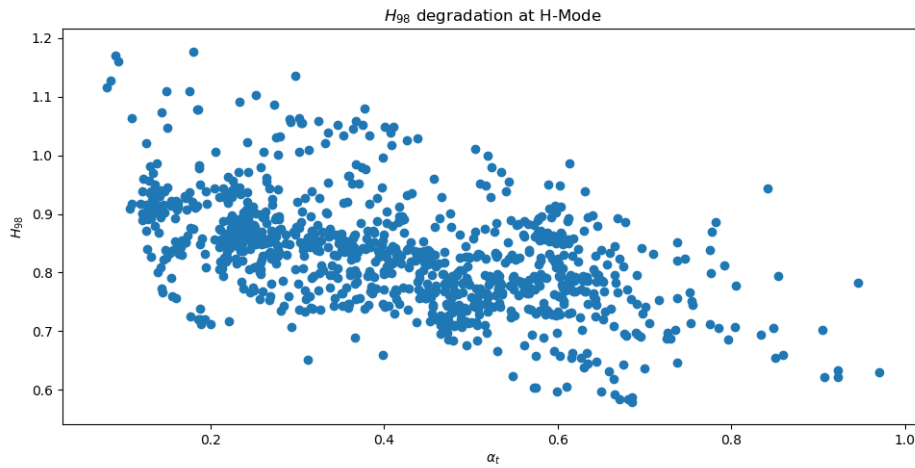


Figure 3.14: H_{98} degradation caused by α_t .

When using α_t as the regression parameter combined with P_{sol} and δ , P_{sol} ceases to have an impact on the degradation compared to the pedestal degradation, which is shown in Fig. 3.15. This finding is of significance since P_{sol} is a common value to correlate edge physics phenomena with core physics, which is represented by H_{98} . Additionally, the quality of the regression increases reasonably with now having a relative RMSE of 6.5%. Furthermore, the influence of α_t itself has reduced as well; it correlates now with the square root of previous correlations. Lastly, the influence of δ remains within the range formed by previous regressions.

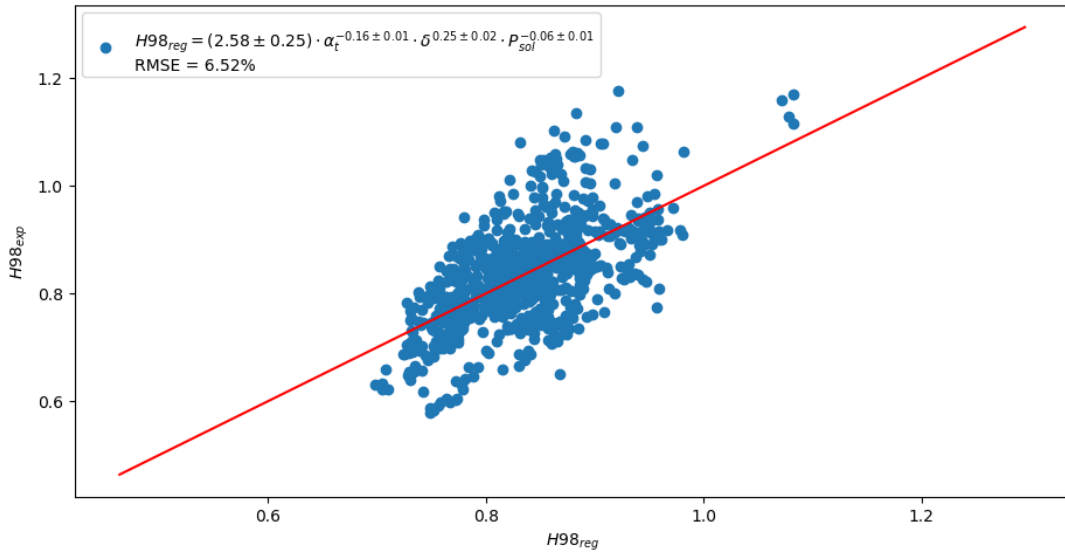


Figure 3.15: Exponential regression of H_{98} with α_t taking into account δ and P_{sol} .

Nonetheless, the influence of α_t is unclear. Therefore, α_t is replaced by its components $T_{e,sep}$ and $n_{e,sep}$ (Fig. 3.16). The quality of the regression remains equally fine. Interestingly, $T_{e,sep}$ only has a very low influence on the H_{98} regression while $n_{e,sep}$ continues to have α_t 's exponent. This indicates that the degradation of H_{98} is mainly induced by the density itself instead of α_t . However, this finding is restricted by the fact that the exponent of δ changes as well, even though α_t does not depend on δ .

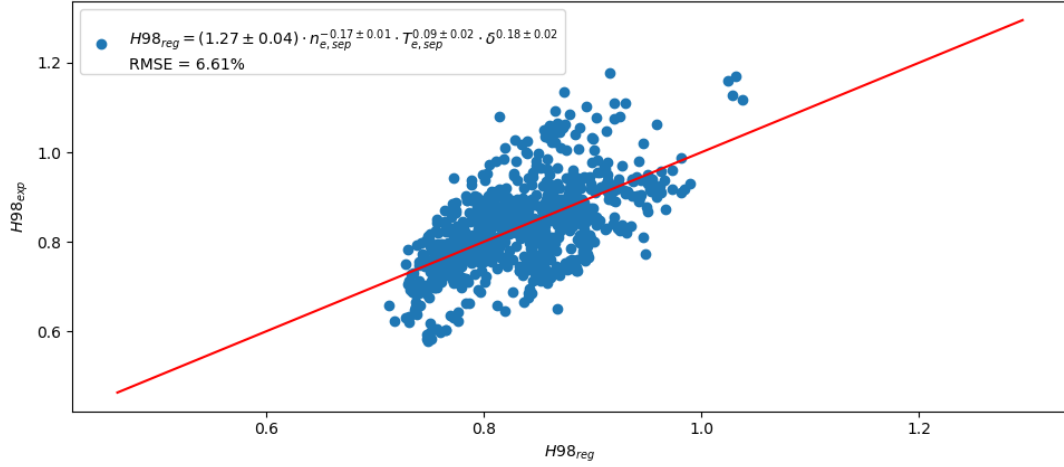
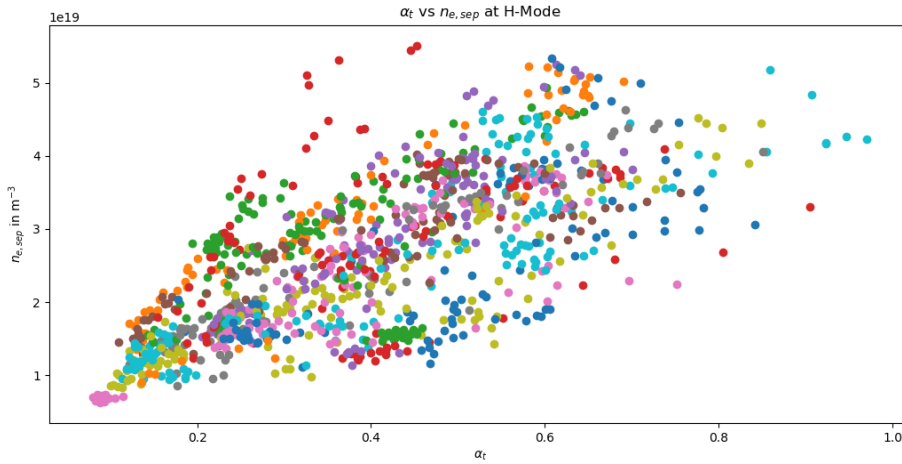


Figure 3.16: Exponential regression of H_{98} with $T_{e,sep}$ and $n_{e,sep}$ taking into account δ .

It is concluded that H_{98} is not a suited parameter to correlate to α_t . While only weak correlations can be observed, no strong correlation is found.

3.2.4 Influence of $n_{e,sep}$ and $T_{e,sep}$ on pedestal degradation

Due to the proportionality $\alpha_t \sim n_{e,sep}/T_{e,sep}^2$ it is of interest whether the pedestal degradation is mainly caused by the electron pedestal temperature or density, which will be object of this section. To that end, in Fig. 3.17 α_t is plotted against both $n_{e,sep}$ and $T_{e,sep}$.



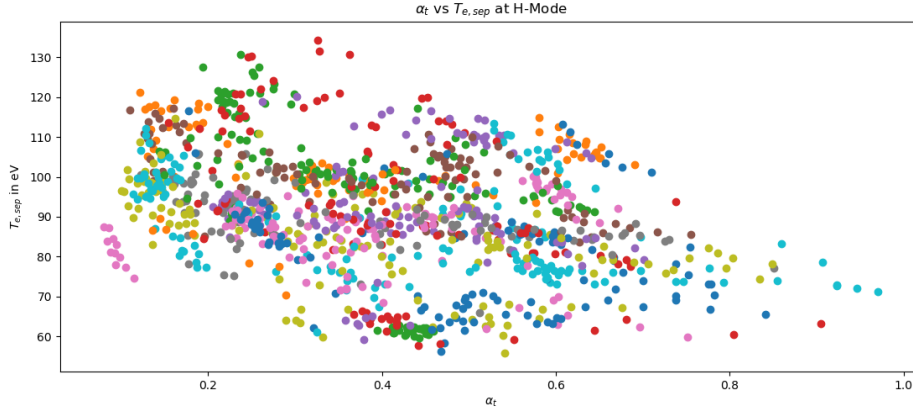


Figure 3.17: Comparison of α_t with $n_{e,sep}$ and $T_{e,sep}$ for H-Mode. Individual colors represent individual discharges from the data base.

As expected, α_t increases with $n_{e,sep}$. Additionally, Fig. 3.17 shows that the data base consists of discharges with broad density scans from $1 \cdot 10^{-19} \text{ m}^{-3}$ to $5 \cdot 10^{-19} \text{ m}^{-3}$, while the temperature remains within $(100 \pm 20) \text{ eV}$. T increases by a factor of approximately two, while n increases by a factor of five. Since $\alpha_t \sim n/T^2$, both quantities exert a similar influence on the turbulence parameter.

In contrast to the density scans performed in Fig. 3.17, the plot in Fig. 3.18 depicts temperature scans performed in discharges # 38742, 38743 and 38744. A temperature scan is obtained by constantly increasing heating power even after the plasma has reached an H-Mode. Different phenomena could lead to an explanation whether or not the pedestal degradation is caused by a variation in $n_{e,sep}$ or $T_{e,sep}$. Again, a pedestal degradation is observed. However, individual shots only show a variation in α_t of about 0.2, which is lower compared to density scans in Fig. 3.17.

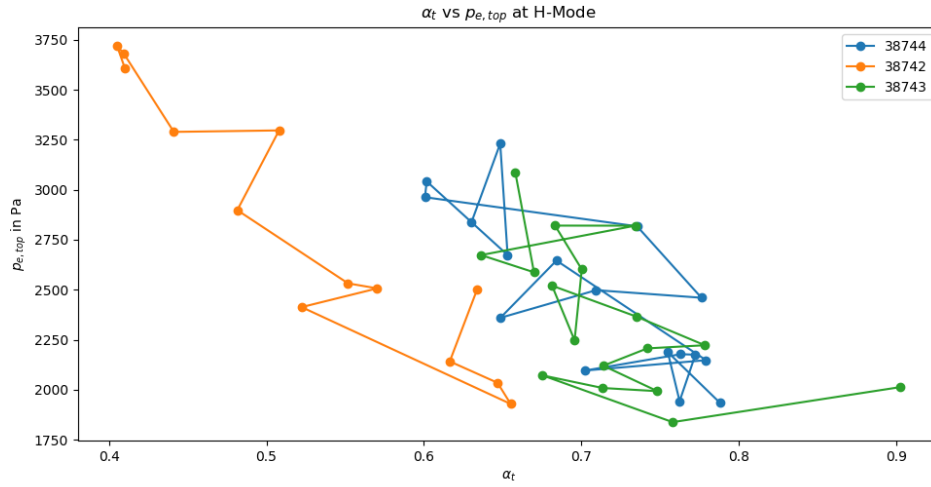


Figure 3.18: Comparison of α_t with $p_{e,ped}$ for H-Mode of temperature scan discharges.

These temperature scans are now compared to a selection of density scan discharges. Fig. 3.19 shows the pedestal degradation of the density scan discharges # 38484, 38485, 38585 and 38589. Each scan shows a broad scan in α_t by starting from values below 0.5 and ending above 0.7. Also, each scan has an α_t range of at least 0.3.

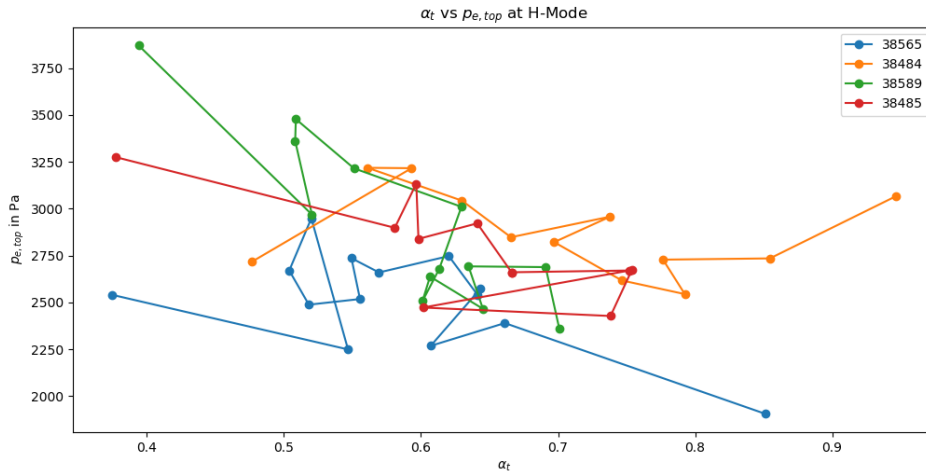


Figure 3.19: Comparison of α_t with $p_{e,ped}$ for H-Mode of density scan discharges.

To understand this deviation, it conveys to look at the distinct influences of both $n_{e,sep}$ and $T_{e,sep}$ in Fig. 3.20.

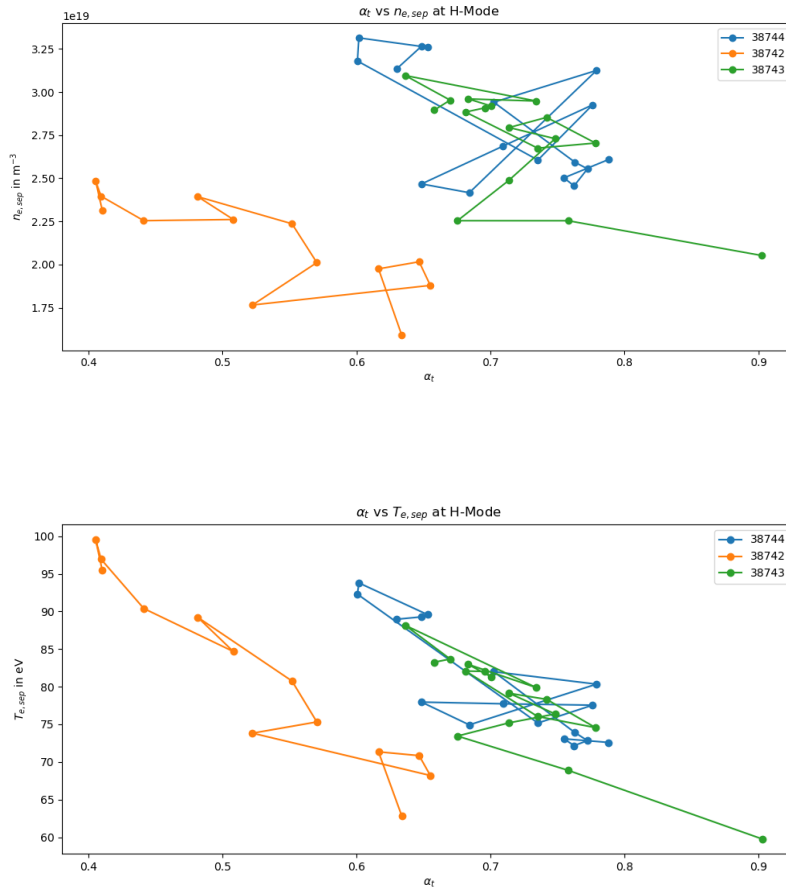


Figure 3.20: Comparison of α_t with $n_{e,sep}$ and $T_{e,sep}$ for H-Mode of temperature scan discharges.

These plots show that an increase in $T_{e,sep}$ of 50% leads to an increase in α_t of 50% as well. Similarly, an increase in $n_{e,sep}$ of 50% leads to an increase in α_t of 50%. This differs to discharges where a density scan is performed. This becomes clear by comparing Fig. 3.20 with a limited number of density scan discharges, Fig. 3.21.

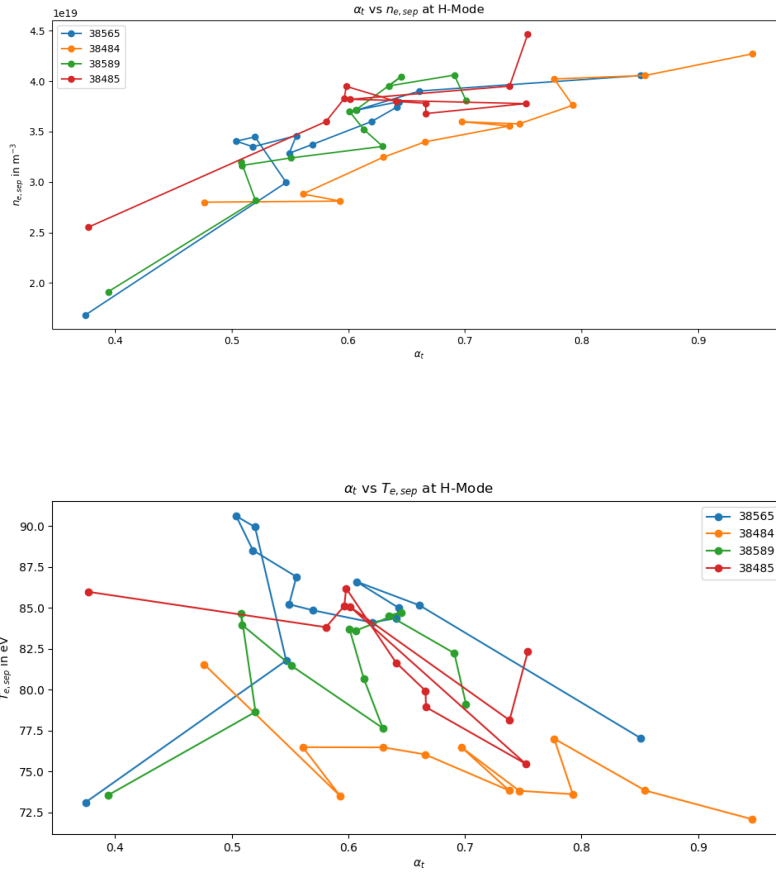


Figure 3.21: Comparison of α_t with $n_{e,sep}$ and $T_{e,sep}$ for H-Mode of density scan discharges.

In these discharges, a change of $n_{e,sep}$ by a factor two leads to an increase of α_t by a factor of shy over two. On the other hand, $T_{e,sep}$ remains almost constant while α_t still increases by a factor of shy over two.

Therefore, it can be concluded that the pedestal degradation caused by an increase in α_t is predominantly due to a change in $n_{e,sep}$. However, the influence of $T_{e,sep}$ cannot be neglected.

3.2.5 Conclusion on α_t dependence for the given data base

Both the electron pedestal top pressure $p_{e,top}$ and the confinement parameter H_{98} degrade with an increase in α_t with a stronger degradation shown for the pressure. Apart from α_t , these degradations are also induced by the triangularity δ and the power transported via the scrape-off-layer P_{sol} . However, regressions could not provide unambiguous explanations on exact correlations between degradations and individual plasma parameters. Additionally, a comparison between temperature and density scan discharges indicates that $n_{e,sep}$ has a more significant contribution on the pedestal degradation than $T_{e,sep}$. Nevertheless, this degradation cannot be reduced to a change in one single parameter.

Chapter 4

Limiting factor two: H-Mode density limit

This chapter compares the four plasma phases describing the H-Mode density limit introduced by [30] with the plasma operational space proposed by [27].

4.1 Theoretical description of density limits

4.1.1 Greenwald-limit and H-Mode density limit

For L-Mode discharges in tokamaks, empirical data showed a limit for the achievable density, the so called Greenwald limit [32]. Therefore, this limit defines the operational space for L-Mode discharges.

$$n_{\text{GW}} = \frac{I_{\text{pol}}}{\pi a^2} \quad (4.1)$$

I_{pol} is the plasma current and a the inner radius of a tokamak. Interestingly, this limit sets into relation three quantities which are not connected by any physical principle. However, it is widely used in plasma physics since 1988.

The Greenwald density limit is an important quantity in plasma physics since it can be used to define the operational space of a fusion machine. For example, ITER has been designed to operate at a confinement factor of $H_{98} = 1$ at $n_e/n_{\text{GW}} = 0.85$ [33].

Fig. 4.1 illustrates this by plotting the core confinement factor H_{98} against the ratio of the electron density to the Greenwald density. As pointed out, ITER is aimed to have a high confinement factor at the Greenwald limit. This is achieved by a high triangularity δ .

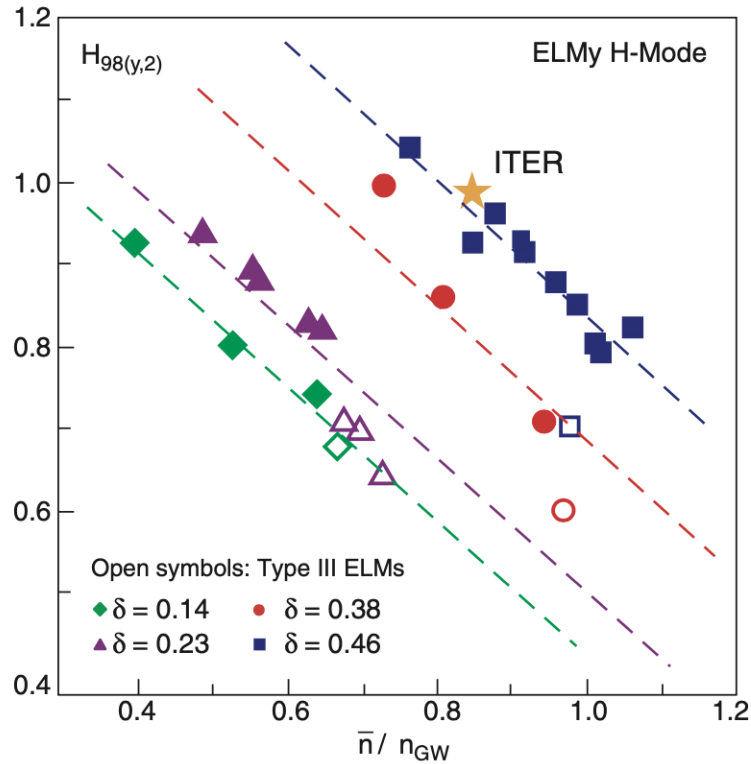


Figure 4.1: Dependence of the confinement factor H_{98} compared to the ratio n_e/n_{GW} and the triangularity δ , adapted from [33].

This limit can be used for H-Modes as well. However, when the plasma density is close to the Greenwald density, confinement gradually decreases, eventually leading to back-transition to L-Mode. Specifically for H-Modes, a similar density limit can be observed, the so called H-Mode density limit (HDL). This limit is - depending on the machine - about 0.8 to 1 times the Greenwald density limit [34]. When an H-Mode reaches this H-Mode density limit, it turns into an L-Mode.

As shown in Eqn. (1.1), the triple product of nuclear fusion depends linearly on n . Since only H-Mode discharges are conceivable for future fusion reactors, the HDL limits their operational space.

Empirically, a scaling for the HDL was found [35]:

$$n_{\text{HDL}} = 48.2 \frac{q_{\perp}^{0.049 \pm 0.041} B_{\text{tor}}^{0.57 \pm 0.08} \delta_{\text{av}}^{0.11 \pm 0.11}}{q_{95}^{0.86 \pm 0.08} R^{1.07 \pm 0.20}} \quad (4.2)$$

n_{HDL} is a line integrated density of unit $[10^{19} \text{m}^{-3}]$, q_{\perp} is the mean power heat flux density across the separatrix in $\frac{\text{MW}}{\text{m}^2}$, δ_{av} the averaged triangularity at the upper and lower divertor. q_{95} the safety factor at $\rho = 0.95$ and R the major radius of the machine in m.

4.1.2 HDL phases

This section focuses on the description of the H-Mode density limit (HDL) following the work of *Bernert*, [30], [36]. *Bernert* proposed four phases that occur when a tokamak is operated close to the HDL. Fig. 4.2 shows the four characteristic phases. It must be noted that not every discharge shows all four phases.

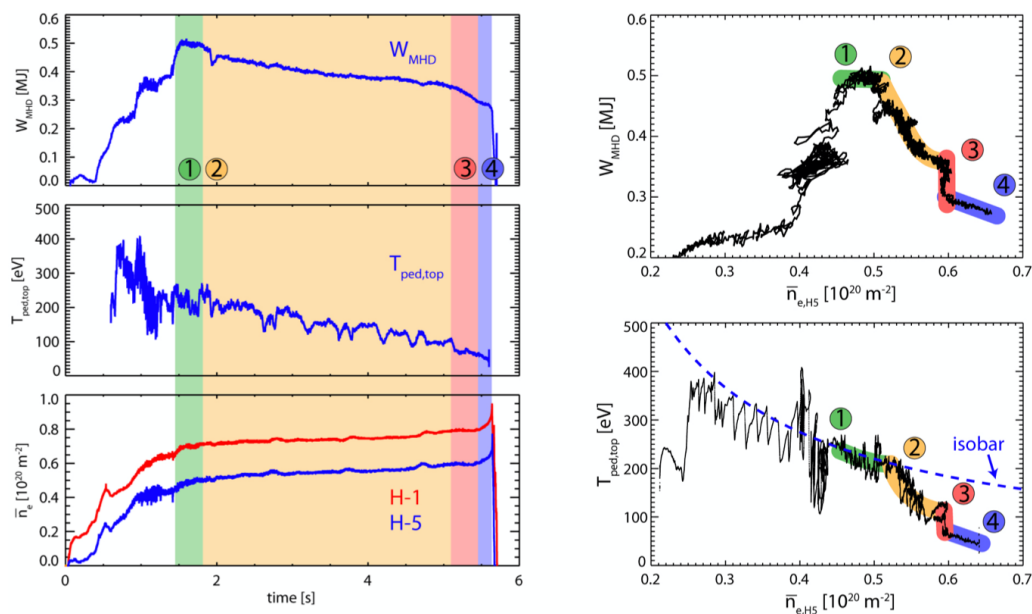


Figure 4.2: Visualisation of four phases at discharge 28728, adapted from [30]. Left: temporal evolution of stored energy W_{MHD} , pedestal top temperature $T_{\text{ped,top}}$ and line integrated density \bar{n}_e . Right: Stored energy compared to integrated line density and pedestal top temperature compared to integrated line density.

Phase 1: Stable H-Mode

The first phase is characterized by constant stored energy while the density increases. Additionally, the pressure remains constant, which can be seen by the isobar in the $n - T$ diagram. Consequently, the confinement stays constant, leading to a stable H-Mode phase. Temperature and density are measured at the pedestal top.

Phase 2: Degrading H-Mode

The stored energy starts to decrease gradually. Simultaneously, an increase in density leads to a conjoint decrease in temperature and pressure, drawing the graph slowly apart from the isobar. As a consequence, the confinement is decreased and the H-Mode is degrading.

Phase 3: H-Mode break down

At a certain density, both energy and pedestal top energy break down. With the drop of the pedestal energy the pedestal gradient reduces, leading to an L-Mode back transition of the H-Mode.

Phase 4: L-Mode

Once the H-Mode is broken down, the plasma continues to exist in an L-Mode. Note that the density can still be increased without major changes in stored energy or pedestal top energy.

4.2 Correlation between phases, separatrix temperature and density

From previous works [27] and [30] it remained unclear, whether or not these different phases have an influence on separatrix temperature and density. For this purpose, a set of thirteen discharges at H-Mode density limit was analyzed. The data base of discharges used in this chapter are found in A.3. Only discharges which were driven to the H-Mode density limit can be used for this analysis.

Firstly, boundaries of the phases must be determined. No numeric method can be applied, each discharge has to be examined individually by hand. To increase difficulty, in some discharges the phases behave differently compared to the phases shown in [30]. For example, instead of a clear drop during phase 3 with respect to energy loss and density, a slowly decreasing density can be observed in discharge 34966 (Fig. 4.3). It must be noted that phase transitions are limited to a temporal resolution of about 100 ms.

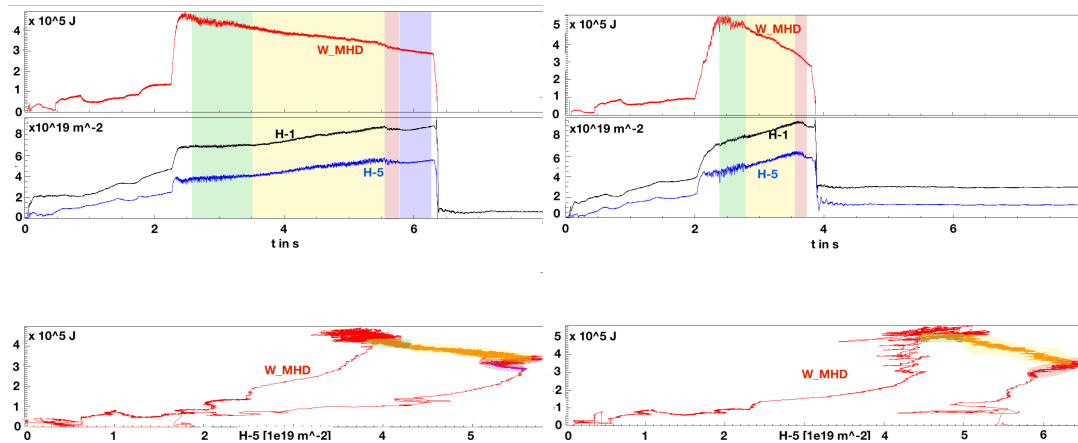


Figure 4.3: Exemplary determination of phases in discharges 34276 (left) and 34966 (right). The top row shows the temporal evolution of plasma stored energy W_{MHD} . The second row depicts the temporal evolution of the integrated edge line density H-5 (blue) and integrated core line density H-1 (black). The last row displays the integrated edge line density on the x-axis in comparison to the plasma stored energy on the y-axis.

A comparison to α_t is not possible for this data base since some of these discharges were seeded with nitrogen gas. This seeding leads to variation in Z_{eff} , which cannot be measured. Still, it is of interest if a correlation between electron separatrix temperature $T_{\text{e,sep}}$, electron separatrix density $n_{\text{e,sep}}$ and these phases exist.

One problem arises from the measuring method of separatrix density and temperature via Thomson scattering. This measuring system has a limited temporal resolution of 500 ms. The data is interpolated and moving average of 50 ms in time and of 2 mm in space to improve quality is calculated.

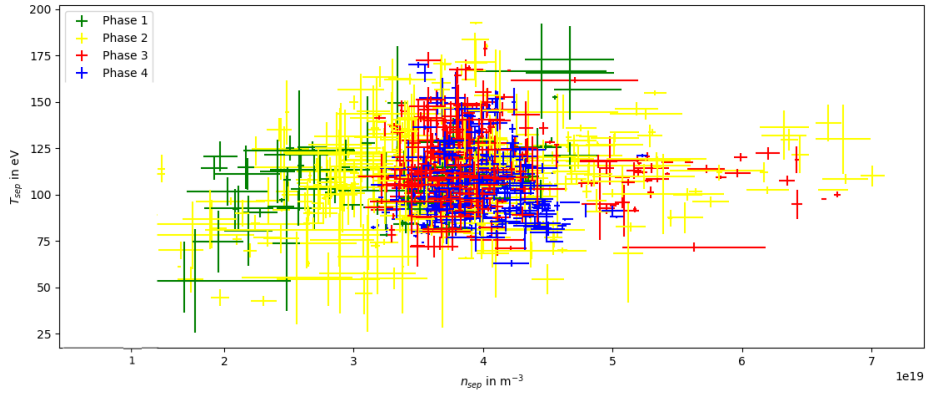


Figure 4.4: Comparison of $T_{e,sep}$ and $n_{e,sep}$ with their respective phase of the entire data base.

As seen in Fig. 4.4, data from all phases scatter throughout all densities and temperatures with an accumulation at $4 \cdot 10^{19} m^{-3}$ and 100 eV. Thus, no findings are derived from the entire data base. To narrow effects from different discharges, the plot is limited to four discharges which are almost identical in their properties such as heating powers, poloidal and toroidal magnetic fields. The result is presented in Fig. 4.5.

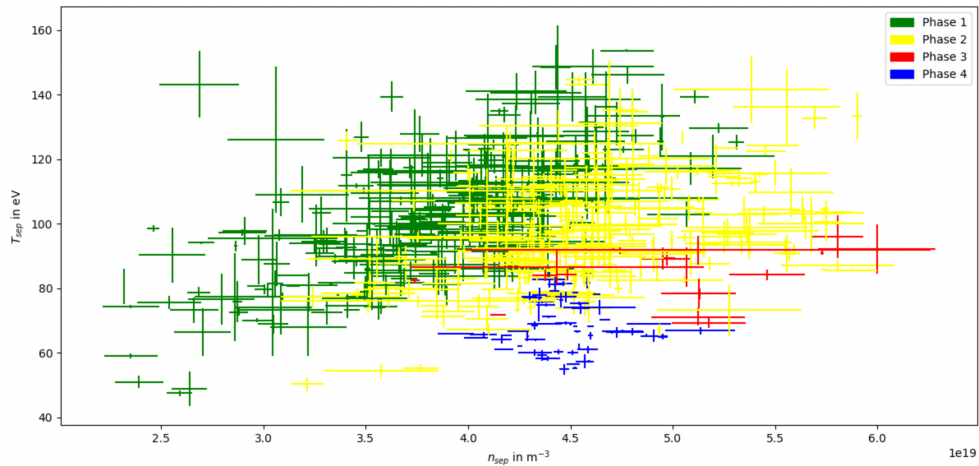


Figure 4.5: Comparison of $T_{e,sep}$ and $n_{e,sep}$ with their respective phase of 38429, 38399, 38484, 38485.

Here, most clearly the four phases appear at different regions. The constant H-Mode (Phase 1) is limited to a triangle on the upper left part of the diagram, representing higher temperatures or higher densities. The degrading H-Mode (Phase 2) has an accumulation

in a strip at slightly higher densities than the stable H-Mode (Phase 1). The breakdown (Phase 3) can be found at higher densities at about 100 eV, while the resulting L-Mode (Phase 4) resides at low temperatures.

Due to resolution limits of Thomson scattering data, no further conclusions are derived. This can be overcome by using ASDEX Upgrade's super fast Helium beam diagnostics (HEB), which can potentially measure both electron temperature and density with high temporal resolution. However, HEB data was not available for this data base.

This plot can be compared to Fig. 3.3 by adding α_t isobars. This is shown in Fig. 4.6.

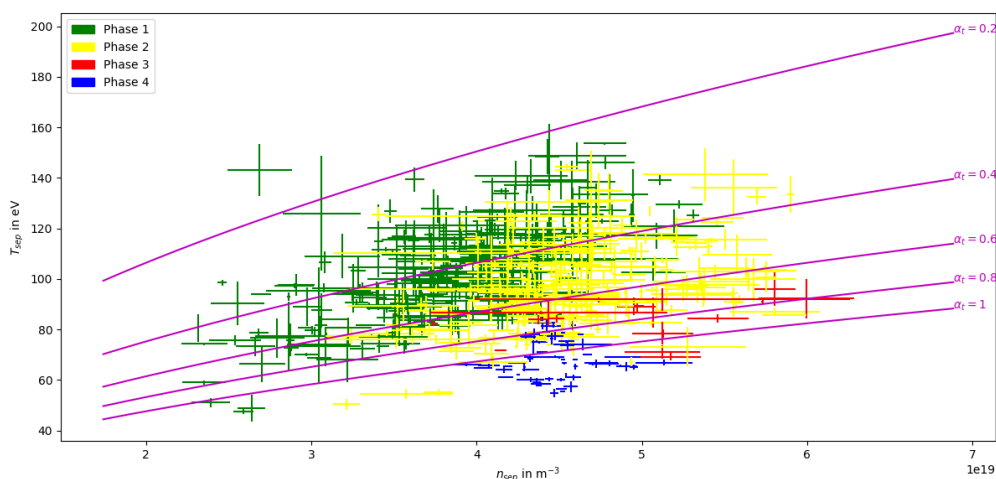


Figure 4.6: Comparison of $T_{e,sep}$ and $n_{e,sep}$ with their respective phases of 38429, 38399, 38484, 38485 with α_t isobars.

Here, the important conclusion is derived that α_t as a parameter is not able to describe different phases. While certain values such as $\alpha_t = 0.2$ are only found at stable H-Modes, other α_t values cross multiple phases. This supports the findings of the previous chapter where α_t could not be generalized to its correlation to confinement properties. However, the assumption that H-Modes cannot sustain at high values of α_t , especially at $\alpha_t > 1$, is verified [16].

Chapter 5

Limiting factor three: Heat flux in the edge

This chapter focuses on the behaviour of heat fluxes in the edge region.

5.1 Theoretical description of heat fluxes

In a plasma, heat is transported due to local differences in temperature and density. The heat flux in a toroidal plasma can be split up in a perpendicular contribution

$$q_{\perp} = -\chi \cdot n \cdot \nabla T - 2.5 \cdot D \cdot T \cdot \nabla n \quad (5.1)$$

and a parallel contribution

$$q_{\parallel} = \frac{640\sqrt{2\pi}\varepsilon_0^2}{e^4\sqrt{m}\Lambda} T^{5/2} \nabla T. \quad (5.2)$$

χ denotes the heat coefficient, D the diffusion coefficient and Λ the Coulomb logarithm. These equations are valid for both electrons and ions with their respective temperatures, densities and heat coefficients.

Due to its dependency on n , T and m , heat fluxes differ between electrons and ions. Between these charged particles, a heat exchange occurs. The exchange term for a

Deuterium plasma is given by

$$Q_{ei} = -3 \frac{m_e}{m_i} n_e n_i k_B (T_e - T_i). \quad (5.3)$$

5.2 Understanding behaviour via simulations

In this chapter, ASDEX Upgrade discharges are simulated with the EMC3-EIRENE code. With these simulations, heat fluxes at the edge can be calculated. Previous works using the TRANSP code [37] considered heat fluxes in the confinement region until $\rho = 0.95$ [38], being limited by the spatial domain covered by TRANSP. This chapter extends the observed volume to the separatrix and SOL.

Specifically, parallel and perpendicular heat fluxes are calculated for both an L-Mode and an H-Mode at different densities and ratios between electron and ion heating.

5.2.1 EMC3-EIRENE

For this research, the EMC3-EIRENE code is used. This code is a combination of the EMC3 and the EIRENE code

EMC3 - short for Edge Monte Carlo 3D - solves the Braginskii equations three-dimensionally by Monte Carlo calculations [39]. This code solves equations for conservation of particles, momentum and energy. The EIRENE code [40], [41] calculates the transport of neutral particles and their interaction with the plasma.

The combination of these codes allows the simulation of stationary plasmas in three dimensions [42]. Furthermore, it grants the opportunity to simulate self-consistently the plasma with impurities and neutral transport realistically for complex field and divertor geometries [43].

5.2.2 Discharges

EMC3-EIRENE requires a predefined grid. For this study, two grids have been used. The L-Mode grid is based on the ASDEX Upgrade discharge # 32922. Characteris-

tic parameters of this discharge are shown in Fig. 5.1. This discharge was heated by 0.25 MW of electron resonance heating, had a toroidal magnetic field of $B_{\text{tor}} = 2.5\text{ T}$ and a plasma current of $I_{\text{pol}} = 830\text{ kA}$.

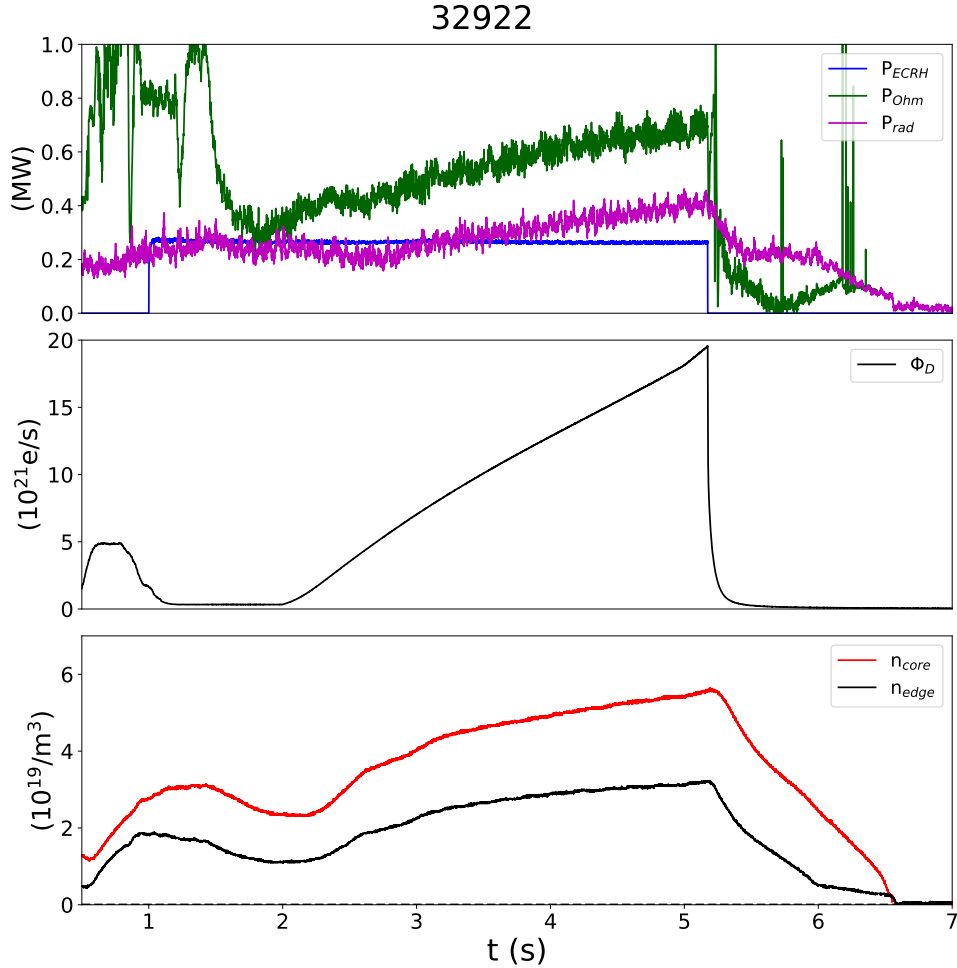


Figure 5.1: Discharge # 32922. Top: Heating power of each heating system (P_{ECRH} and P_{Ohm}) and radiated power P_{rad} . Middle: Deuterium puffing rate Φ_D . Bottom: Density at the edge and in the core.

H-Mode simulations are based on discharges # 38484 and # 38485. Characteristic parameters are depicted in Fig. 5.2. Both discharges are identical in its physical parameters, they only differ in its position of their magnetic equilibrium within the vacuum vessel by 13 mm due to diagnostic reasons. These discharges are powered by 2.5 MW

of neutral beam injection with a ramp at the end. A ramp is induced by turning the neutral beam heating (NBI) on and off periodically. The frequency of the NBI heating being on is steadily reduced. As a result, on average the NBI heating power is reduced. This ramp triggers a back-transition to L-Mode. The toroidal field of these discharges was set to $B_{\text{tor}} = -2.4 \text{ T}$ and the plasma current accounted to $I_{\text{pol}} = 830 \text{ kA}$.

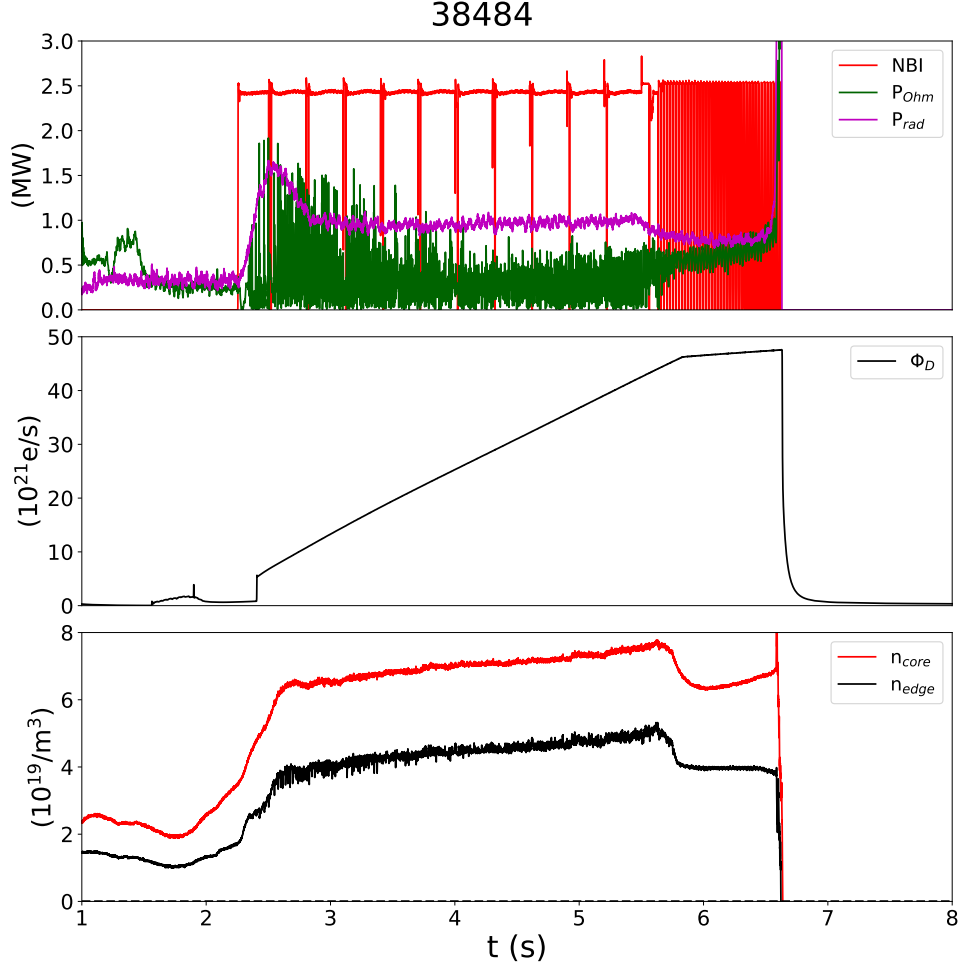


Figure 5.2: Discharge #38484. Top: Heating power of each heating system (NBI and P_{Ohm}) and radiated power P_{rad} . Middle: Deuterium puffing rate Φ_D . Bottom: Density at the edge and in the core.

Based on these grids, two pairs of studies are conducted. First, L-Modes with $P_{\text{heat}} = 0.8 \text{ MW}$ are simulated with separatrix densities $n_{\text{sep}} \in \{0.5, 1, 1.5, 2, 2.5, 3\} \cdot 10^{19} \text{ m}^{-3}$.

This heating power differs from the heating power of the L-Mode on which the grid is based. The goal is to simulate a typical L-Mode. The grid of # 32922 is used due to the fact that this grid was already created for other simulation studies. However, the heating power needed to be adapted. Second, H-Modes with $P_{\text{heat}} = 2.5 \text{ MW}$ are simulated with separatrix densities $n_{\text{sep}} \in \{0.5, 1, 1.5, 2, 2.5, 3, 3.5, 4, 4.5, 5, 5.5, 6\} \cdot 10^{19} \text{ m}^{-3}$.

At each density step, five different simulations are performed. Between these simulations, the ratio between heating of the electrons and ions is modified to 10:90, 30:70, 50:50, 70:30 and 90:10. These ratios are used since the exact relations in a experiment are unknown. By simulating this wide range, we can take the effect of the heating into account. Plots for the 30:70 and 70:30 cases can be found in appendix B. For simplicity, the heating ratio R is defined as

$$R = \frac{P_{\text{heat,e}}}{P_{\text{heat,i}}} \quad (5.4)$$

with $P_{\text{heat,e}}$ describing the power used to heat electrons and $P_{\text{heat,i}}$ the power used to heat ions.

5.2.3 Determining heat and diffusion coefficients

As seen in Eqn. (5.1), it is important to determine heat and diffusion coefficients.

For L-Mode discharges, spatially constant heat and diffusion coefficients are assumed. They are determined by adapting the input transport coefficients in the simulation until it fits experimental data for temperatures. This is shown by Fig. 5.3. For this purpose, it is assumed that electrons and ions were heated equally in the experiment. This assumption is in accordance with [5] and the observation that the heat coefficient profiles match for profiles with different heating power correlations. Due to nitrogen seeding, the coefficients could not be tuned for density.

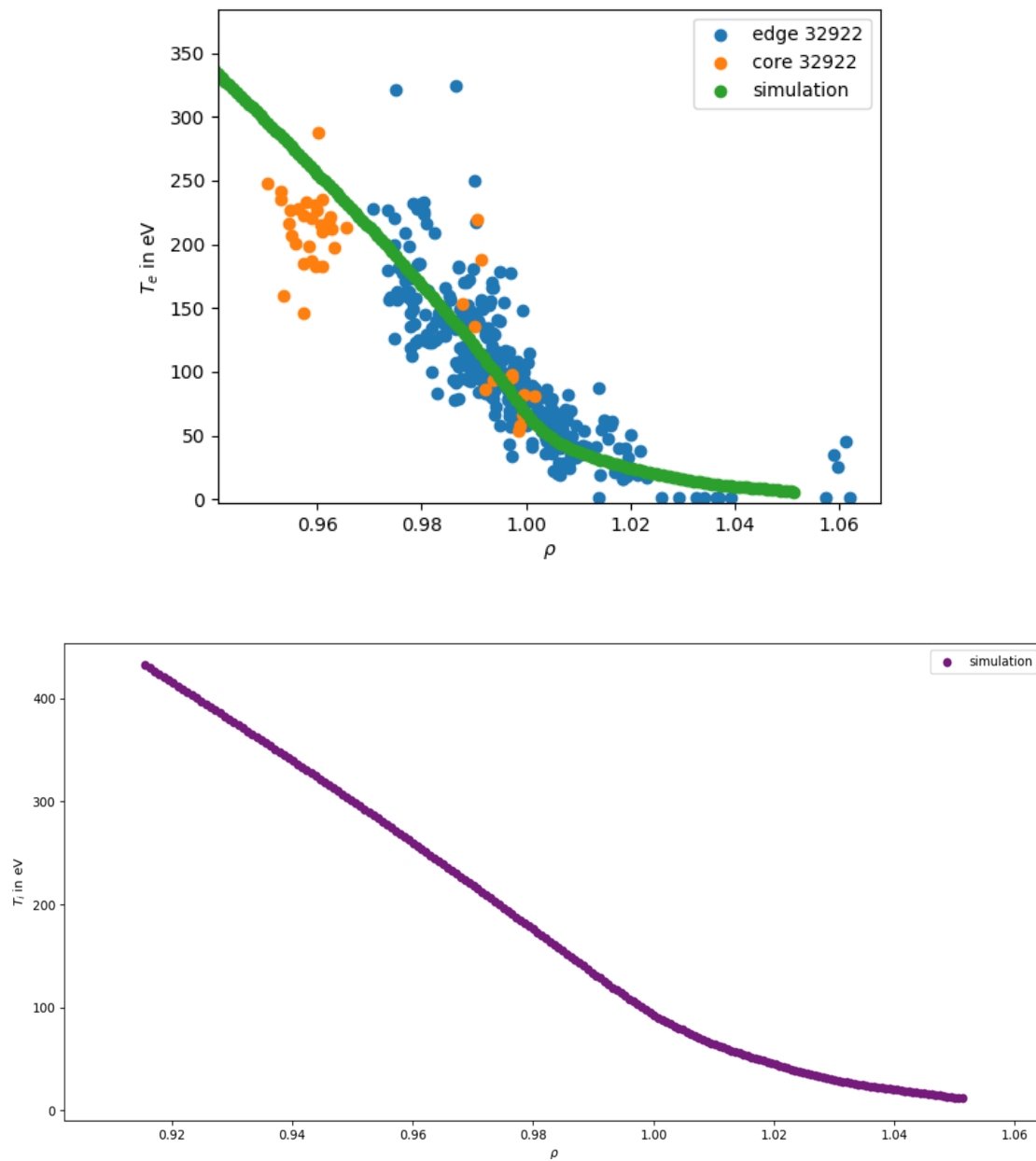


Figure 5.3: Discharge #32922. Top: Electron temperature of the simulation (green, $n = 2.5 \cdot 10^{19} \text{ m}^{-3}$) compared to Thomson scattering electron temperature measurements (blue and orange). Bottom: Ion temperature of the simulation (violet). For discharge 32922 no experimental ion temperature data is available.

Since no experimental data of T_i is available, $\chi_e = \chi_i$ is assumed. This results in:

$$\chi_e = 0.5 \frac{\text{m}^2}{\text{s}} \quad (5.5)$$

$$\chi_i = 0.5 \frac{\text{m}^2}{\text{s}} \quad (5.6)$$

$$D = 0.15 \frac{\text{m}^2}{\text{s}} \quad (5.7)$$

H-Modes are characterized by a pedestal. This pedestal is caused by a heat barrier, which needs to be accounted for in the heat coefficient profile. The heat coefficients are depicted in Fig. 5.4.

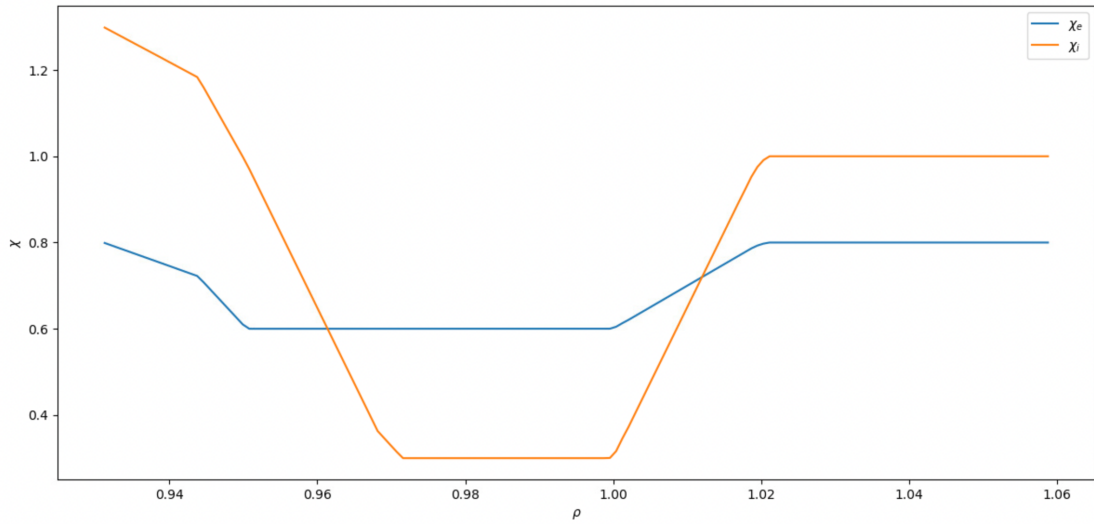


Figure 5.4: Heat coefficient for H-Mode discharges in $\frac{\text{m}^2}{\text{s}}$.

D is set to $D = 1/3\chi_e$.

These profiles fit to experimental data independent of the correlation between heating powers. For electron temperature, this is shown in Fig.5.5 and for electron density in Fig. 5.6.

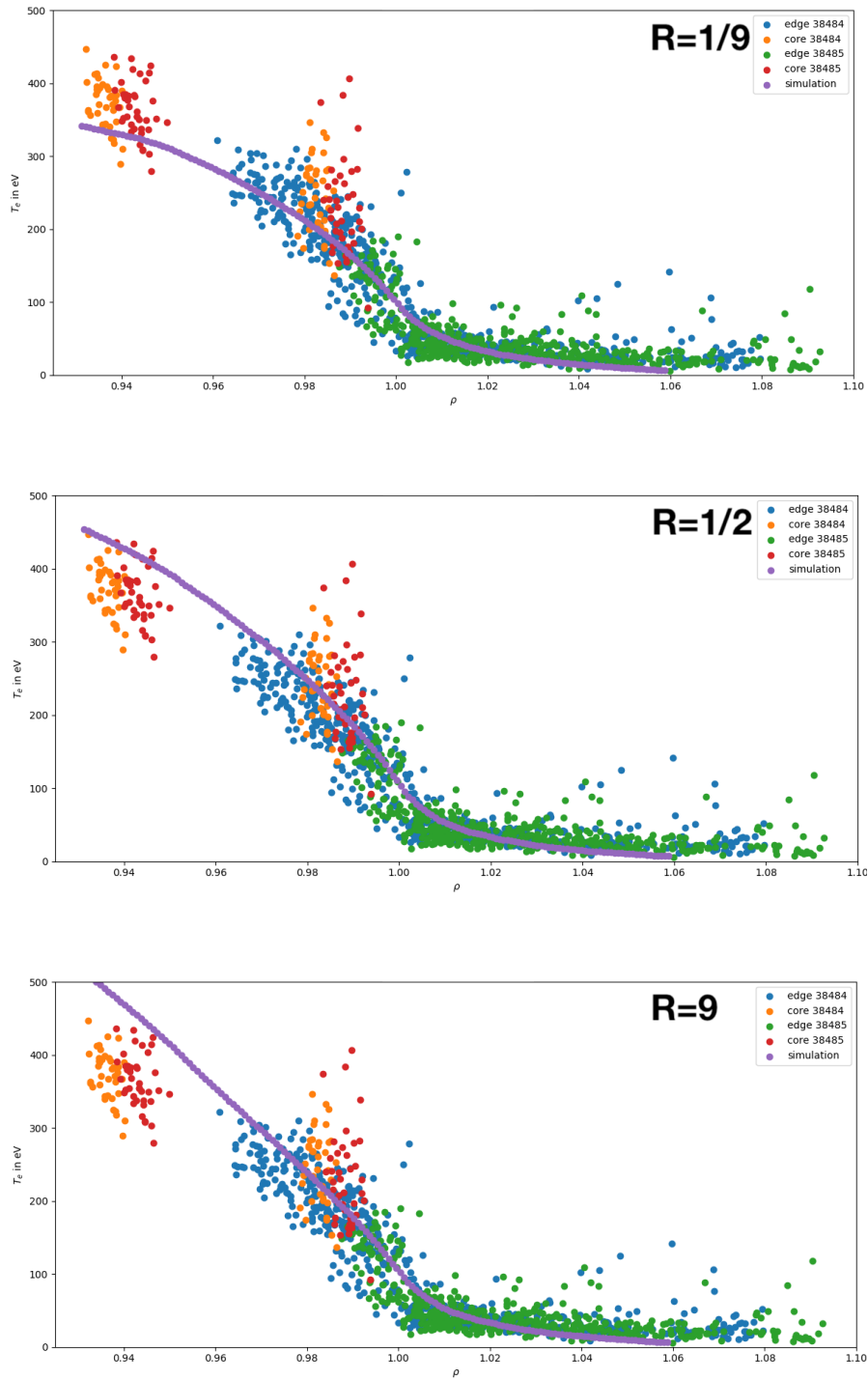


Figure 5.5: Discharges #38484 and 38485. Comparison between Thomson data of electron temperature with simulations with $n = 4 \cdot 10^{19} \text{ m}^{-3}$.

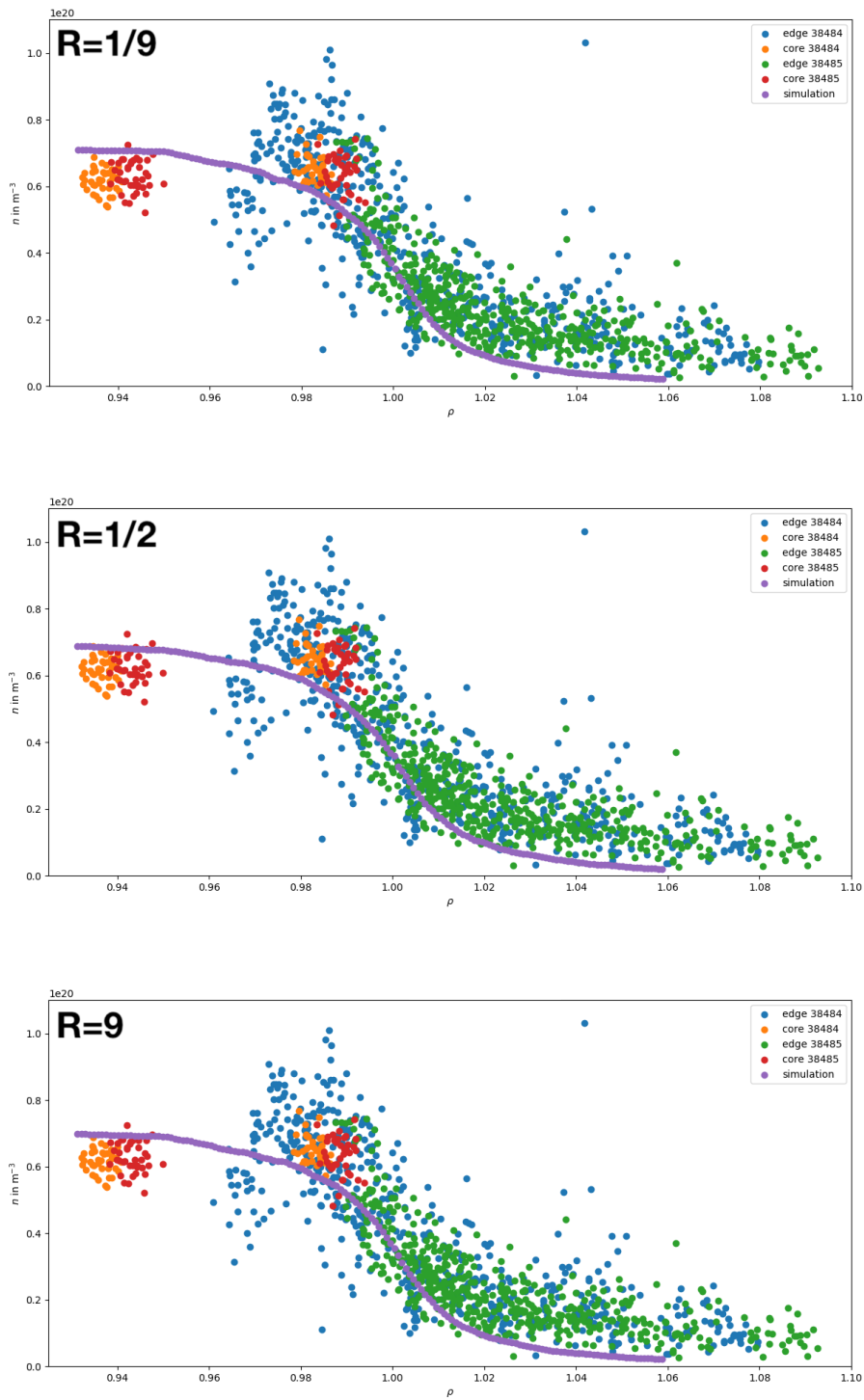


Figure 5.6: Discharges # 38484 and 38485. Comparison between Thomson data electron density with simulations with $n = 4 \cdot 10^{19} \text{ m}^{-3}$.

Additionally, the simulated ion temperature profile matches well with the experimental one as seen in Fig. 5.7.

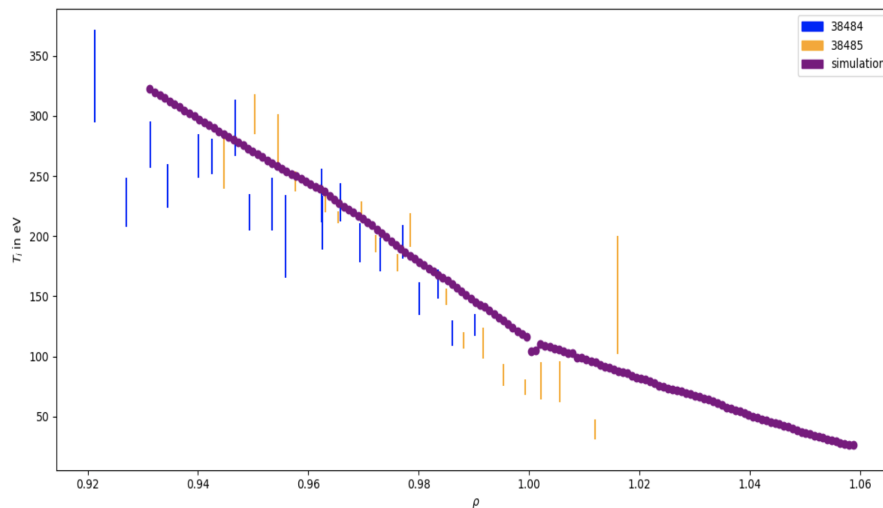


Figure 5.7: Discharges #38484 and 38485. Comparison between data of ion temperature (CMZ diagnostics) with simulation at $n = 4 \cdot 10^{19} \text{ m}^{-3}$ and equally distributed heating power. The dip near the separatrix is caused by Monte Carlo noise.

Furthermore, these heat coefficients replicate the density curve of the experimental data at different densities. This is shown in Fig. 5.8.

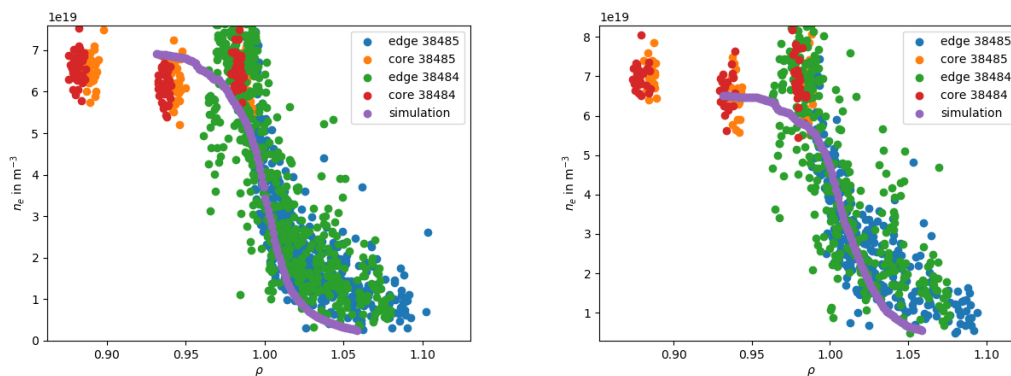


Figure 5.8: Discharges #38484 and 38485. Comparison between data of electron density (Thomson diagnostics) with simulations at $n = 4 \cdot 10^{19} \text{ m}^{-3}$ (left) and $n = 5 \cdot 10^{19} \text{ m}^{-3}$ (right) with an electron to ion heating ratio of $R = 1/2$.

5.2.4 Heat transport within confinement region

In this section, heat transport within the confinement region, i.e. $0.93 \leq \rho \leq 1$, is analysed.

Heat transport from inner boundary to separatrix

First, it is examined how heat is transported from the inner simulation boundary ($\rho = 0.93$) to the separatrix ($\rho = 1$). Within the confinement region, heat is mainly transported by a perpendicular heat flux, the parallel component is negligible. For this purpose, simulation data is normalized to the total heat flux crossing the separatrix:

$$\frac{Q_{e,sep}}{Q_{sep,total}} = \frac{Q_{e,sep}}{Q_{e,sep} + Q_{i,sep}} \quad (5.8)$$

This quantity corresponds to the percentage of the contribution of electrons to the total separatrix heat flux. From the perspective of ions, this corresponds to:

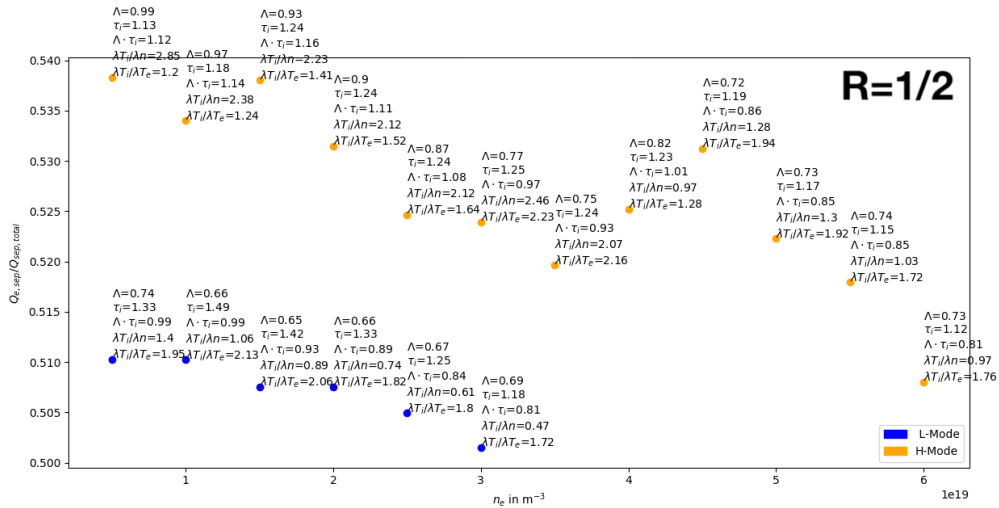
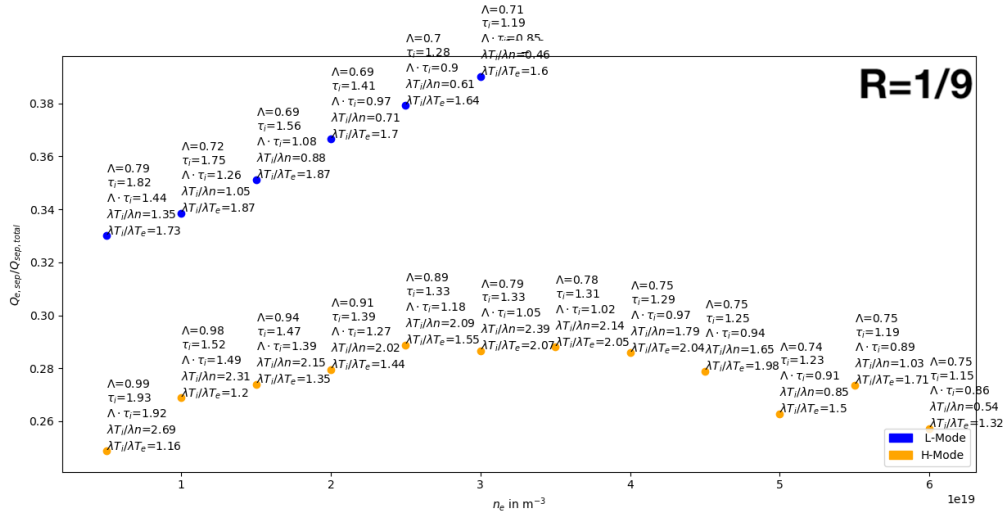
$$\frac{Q_{i,sep}}{Q_{sep,total}} = 1 - \frac{Q_{e,sep}}{Q_{sep,total}} \quad (5.9)$$

In Fig. 5.9 the heating ratio remains fixed for each subplot. Since the heating ratio is known and the total heat flux remains almost constant, the heat exchange between the inner simulation boundary and the separatrix can be deduced by comparing that ratio to the percentage in electron heat flux at the separatrix. It must be kept in mind that the following analysis of H-Modes is based on simulation data which used heat coefficients which were determined at densities of $n_{sep} = \{4.0, 4.5, 5.0\} \cdot 10^{19} \text{ m}^{-3}$. These heat coefficients are held constant for all other densities.

Regarding the $R = 1/2$ case, almost no exchange between ions and electrons take place. A numerical error of about 5 % is assumed. Looking at the extreme case of heating almost only ions, electrons are heated significantly on their way to the separatrix. Due to the large difference in heating, this is expected. Nevertheless, no significant difference between L-Mode and H-Mode or between densities can be observed. In contrast, if almost only electrons are heated, ions gain heat on their way to the separatrix. The factor by which ions are heated, remains approximately constant as well. Compared to the

other extreme case, very hot electrons heat relatively cold ions less than very hot ions heat relatively cold electrons.

Looking at Eqn. (5.3) this similarity between electron and ion heat fluxes in the extreme cases is not expected. The code works with the usual assumption of quasi-neutrality $n_e = n_i$. Even though $m_e \ll m_i$, a heat exchange is expected to occur at significant differences between T_i and T_e . Since the extreme cases show no drastic increase in heat flux, the influence of the exchange term is not significant.



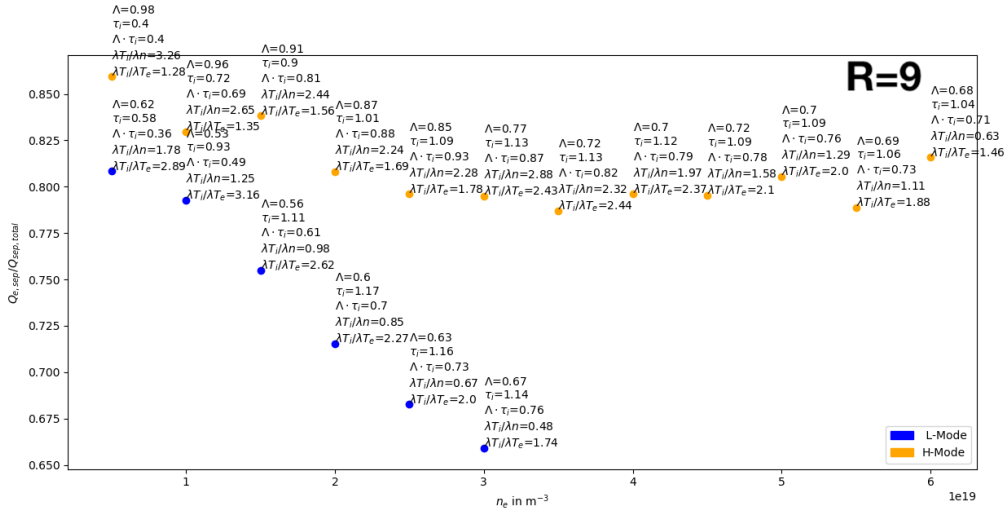


Figure 5.9: Percentage of electron heat flux crossing the separatrix at different densities at H-Mode and L-Mode annotated with temperature and decay length ratios as defined in Eqns. (5.10) and (5.11).

Heat exchange at the separatrix

This section focuses on the heat exchange between electrons and ions. Results are shown in Fig. 5.9. Regarding the extreme cases with a heating ratio of 10:90 ($R = 1/9$ or $R = 9$), it can be seen that the less heated particle type is heated by the respective other type. When mainly ions are heated ($R = 1/9$), electrons are subsequently heated by the ions. In this case at the separatrix, about 25 to 40 % of the heat flux is in electrons, leading to a significant gain of heat by the electrons. The heat exchange to electrons in this case is slightly higher for L-Modes than for H-Modes.

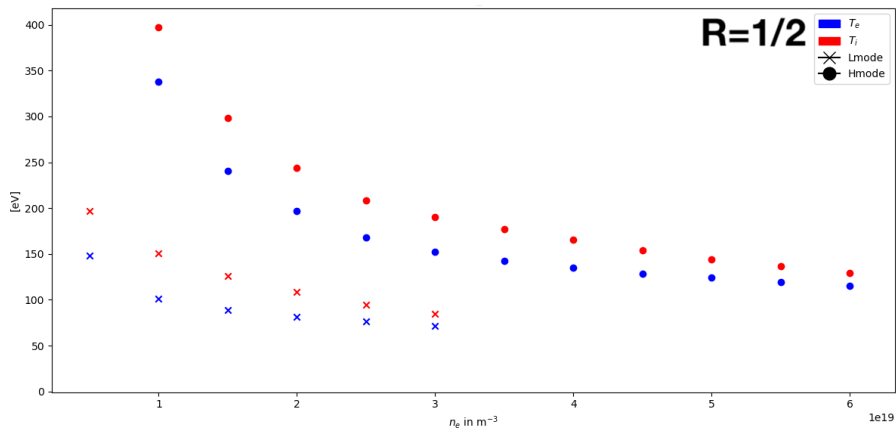
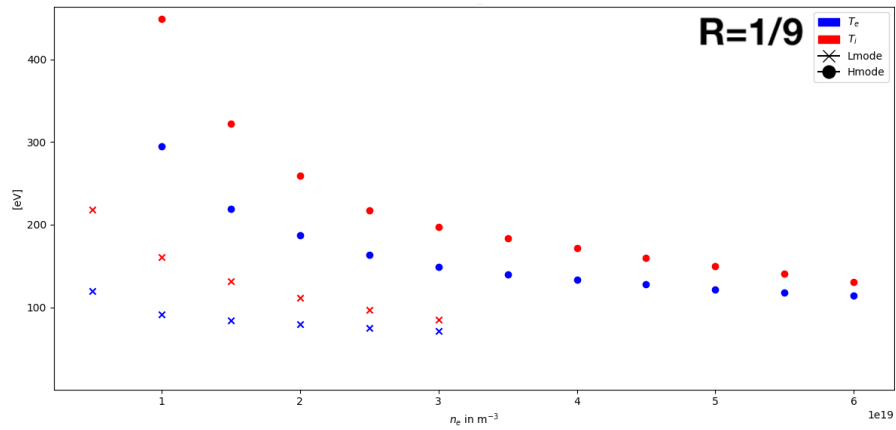
In the contrary case of electrons being mainly heated, ($R = 9$) between 15 and 35 % of the heat flux is in the ions. This exchange is therefore similar to the case of dominant electron heating ($R = 1/9$). The exchange in L-Modes is larger than in H-Modes.

Concerning the case of equal heating, almost no heat exchange takes place. Fig. 5.9 indicates a slight increase of heat flux in electrons of 0.5 to 5 %, but it should be noted that this deviation lingers within a numeric error.

The next step is to analyse quantities which are directly calculated by the simulations.

Separatrix temperatures

This section focuses on electron and ion temperatures at the separatrix. Even though the heat transport is not largely affected by the exchange term, ions are hotter at the separatrix than electrons independent of the heating ratio. This is shown in Fig. 5.10



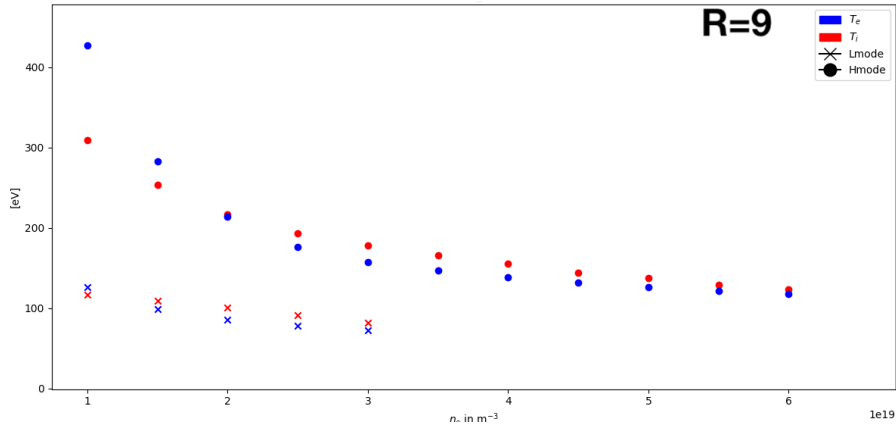


Figure 5.10: Electron and ion temperature at separatrix for L-Mode and H-Mode simulations at different densities. For H-Modes at $n = 0.5 \cdot 10^{19} \text{ m}^{-3}$ no reliable data can be given due to numerical reasons.

It must be noted that separatrix temperatures for L-Modes tend to be high due to a relatively high heating power of 0.8 MW assumed in the simulations. Additionally, H-Modes at $n = 0.5 \cdot 10^{19} \text{ m}^{-3}$ and $n = 1.0 \cdot 10^{19} \text{ m}^{-3}$ are experimentally almost impossible to achieve. Therefore, the simulation data for these simulations should not be overinterpreted.

Decay lengths

This section focuses on decay lengths of temperatures and density at the separatrix. They are calculated by an exponential fit within the interval $[R_{\text{sep}} - 4.5 \text{ mm}, R_{\text{sep}} + 5.5 \text{ mm}]$; a method used in [16]. Corresponding to higher ion temperatures in all heating ratios, Fig. 5.11 shows that decay lengths of ion temperatures are higher than those of electron temperatures.

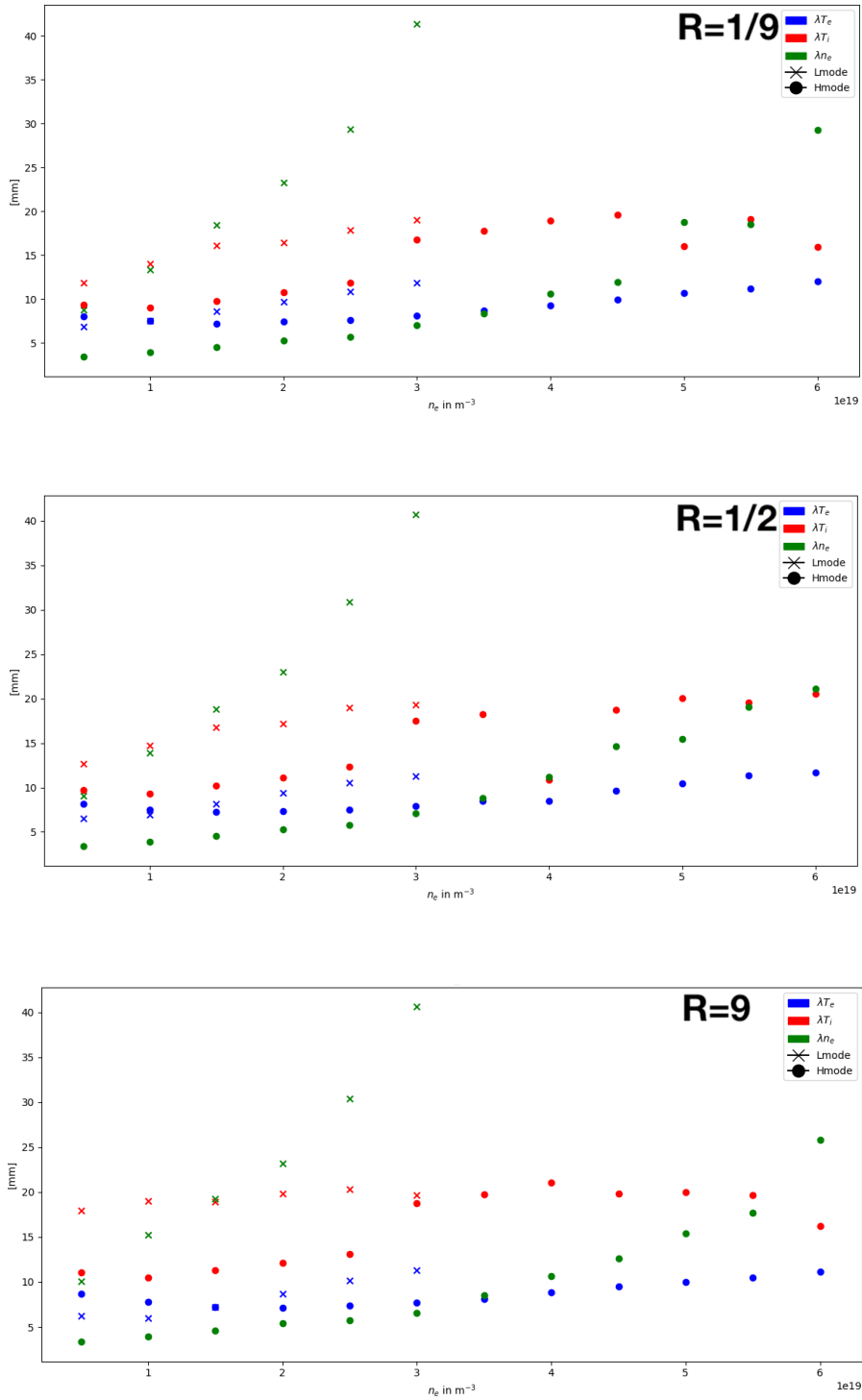


Figure 5.11: Decay lengths of electron and ion temperature as well as electron density for L-Mode and H-Mode at different densities.

However, no significant influence of density, heating relation or confinement mode on decay lengths can be detected. Regardless of these factors, decay lengths for electron temperatures, λ_{T_e} , are between 5 and 10 mm. Decay lengths for ion temperatures, λ_{T_i} , are between 10 and 20 mm. Thus, temperature decay lengths for ions are about twice as high as those for electrons.

Regarding decay lengths of the electron density, λ_{n_e} , a difference between L-Modes and H-Modes can be observed. While λ_{n_e} increases in L-Modes for higher densities exponentially, the increase for H-Modes is linearly. One explanation is that the ratio between perpendicular and parallel heat flux is different since the heat coefficients differ. Especially, in L-Mode simulations $\chi_e = \chi_i$ was assumed. However, the ratio between these heat fluxes determine the width of λ_n . In total, λ_{n_e} is higher for L-Modes than for H-Modes.

Ratios of temperatures and decay lengths

After having analysed temperatures and decay lengths separately, this section focuses on ratios between them. To set different decay lengths into comparison, following parameters are used:

$$\tau_i = \frac{T_{i,sep}}{T_{e,sep}} \quad (5.10)$$

$$\Lambda = \frac{\lambda_{p_e}}{\lambda_{p_i}} \quad (5.11)$$

Since $n_e = n_i$, $\Lambda = \lambda_{T_e}/\lambda_{T_i}$.

As shown before, ion temperatures are slightly higher at the separatrix with no regard to the heating ratio. However, the difference is limited in all simulations to a factor of two where ions are predominantly heated and reduces to a factor of about ten percent in the case of higher density H-Modes where electrons are predominantly heated. This is shown in Fig. 5.12.

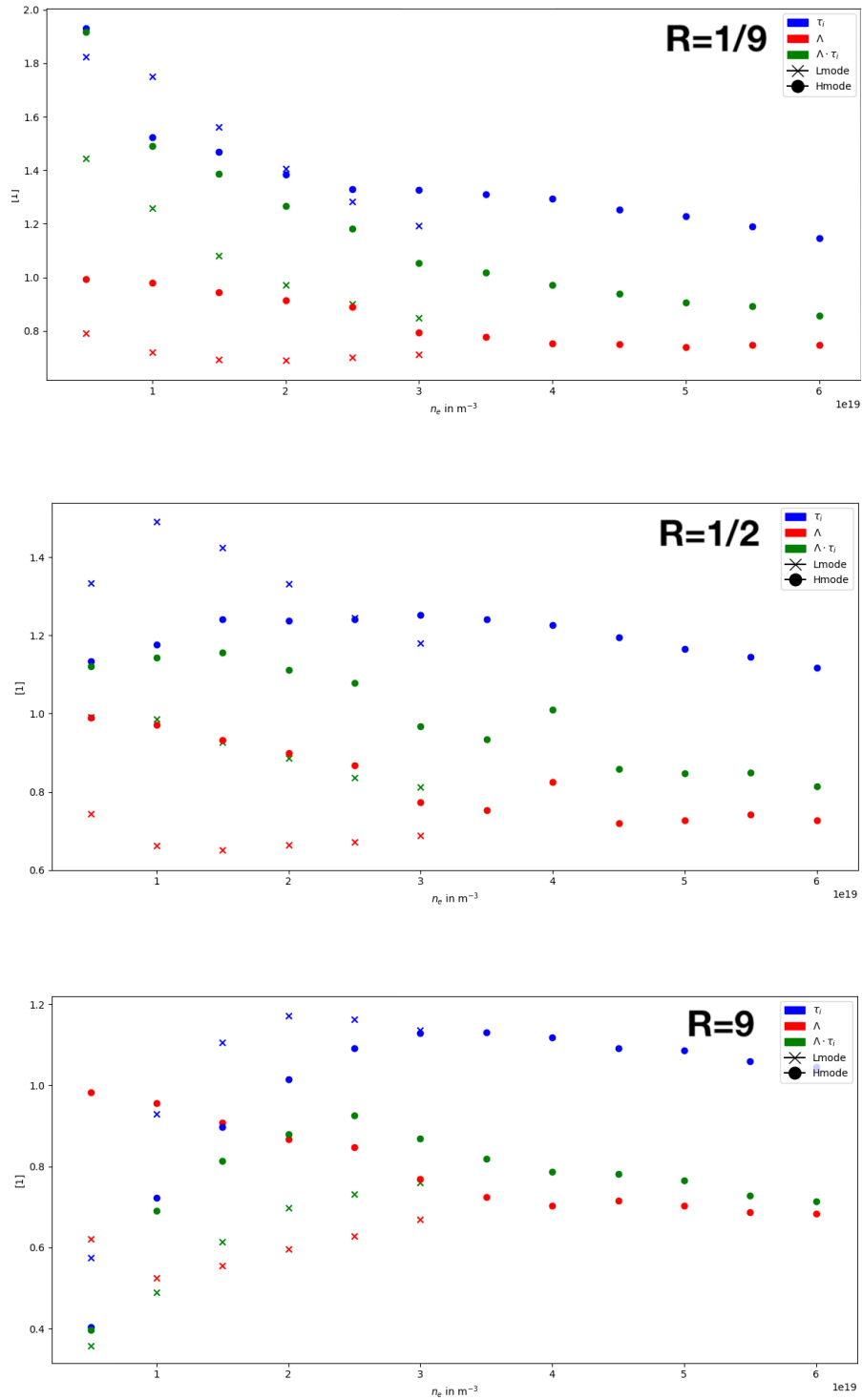


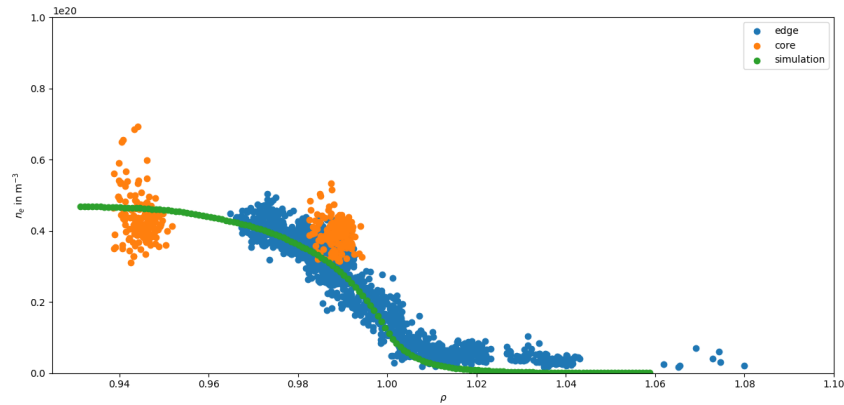
Figure 5.12: Product of Λ and τ_i at L-Mode and H-Mode at different densities.

On the one hand, Λ is below one for all simulations, i.e. λ_{T_e} is always smaller than λ_{T_i} . On the other hand, τ_i is greater than one for each simulation and Λ is smaller than one. Interestingly, the product of these two quantities is close to one in each simulation. This product is slightly above one when ions are predominantly heated, since this leads to a higher difference in electron and ion temperature, thus a higher τ_i . When electrons are predominantly heated, this product is slightly below one. However, for typical H-Modes in the range of $3.0 \cdot 10^{19} \text{ m}^{-3} < n < 4.5 \cdot 10^{19} \text{ m}^{-3}$ this product is very close to one independent of the heating ratio.

Heat coefficients determined at lower densities

The next step is to compare these findings with a low density H-Mode. The simulation grid and parameters are based on discharge #36021. This discharge has a separatrix density of $n_{\text{sep}} = 1.6 \cdot 10^{19} \text{ m}^{-3}$ and a heating power of $P_{\text{heat}} = 0.7 \text{ MW}$.

First, new heat and diffusion coefficients are adapted to the low density H-Mode, Fig. 5.13.



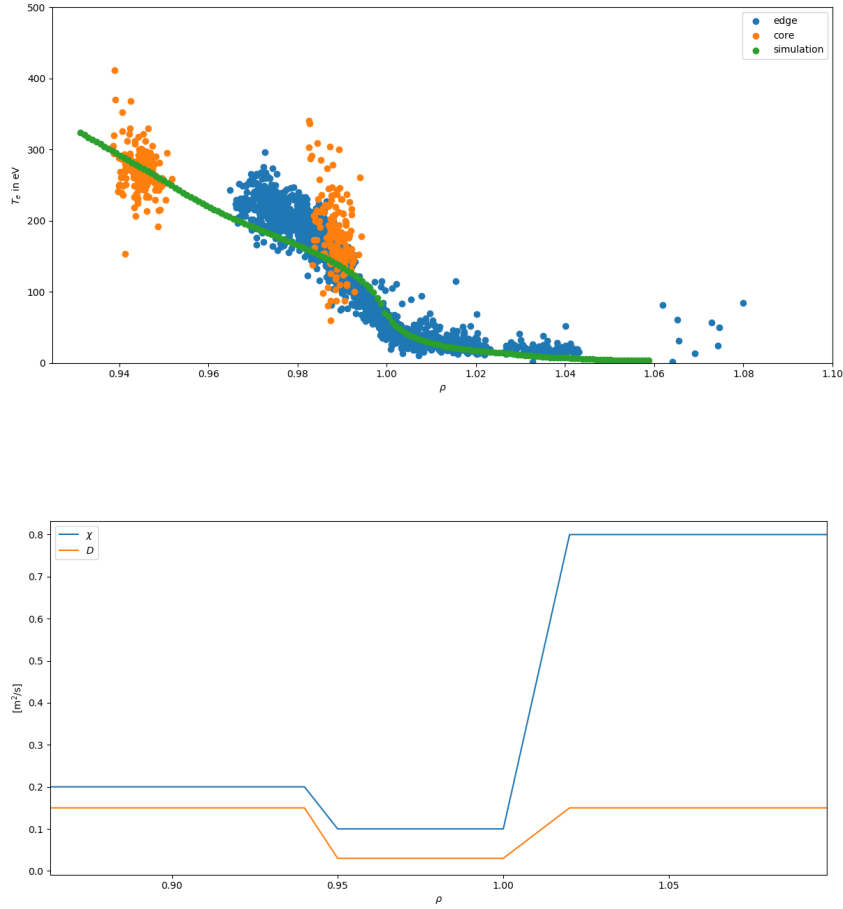
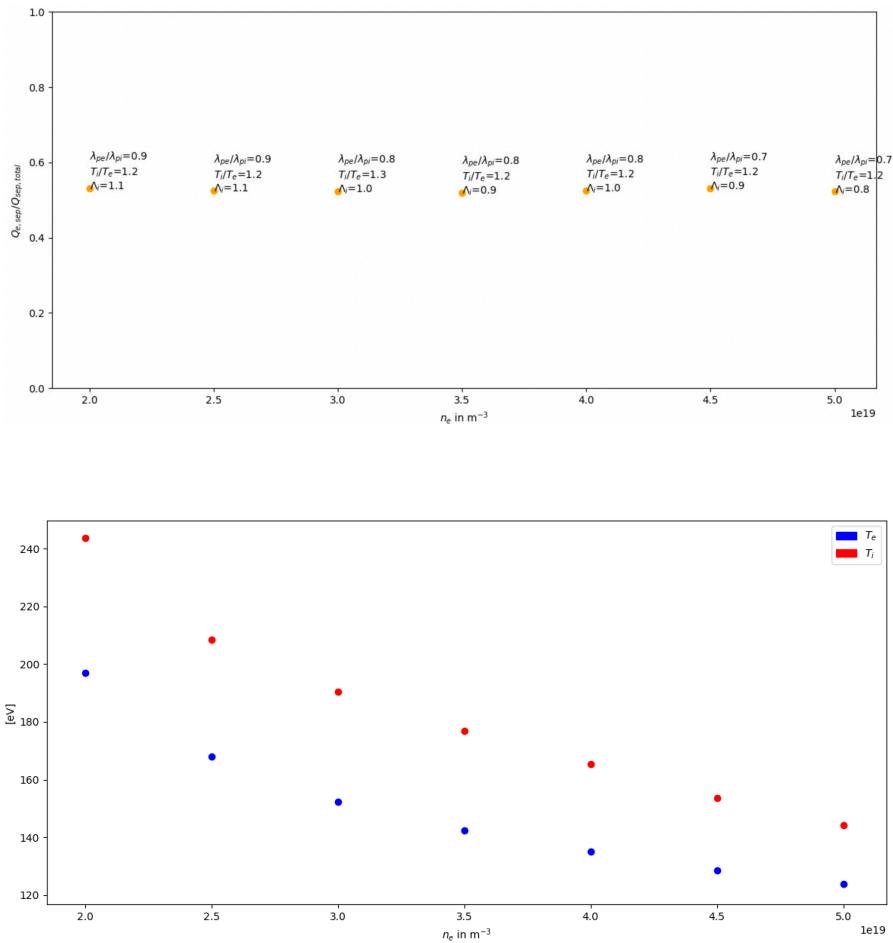


Figure 5.13: Discharge #36021: Concordance between simulation and experimental data for density (top) and electron temperature (middle) for the determined χ and D profiles (bottom). For this discharge, experimental data for ion temperature is not available. Therefore, χ_i is set to be equal to χ_e .

Comparing the heat coefficients between the low density H-Mode #36021 and the standard density H-Modes #38484 and 38485, a reduction of the density by a factor of two leads to a decrease of χ_i by a factor of three and of χ_e by a factor of six. It must be noted that this conclusion should be treated with caution since $\chi_i = \chi_e$ is assumed as a result of a lack of experimental ion data for #36021. However, a correlation with α_T can be observed. A rough estimation of $\alpha_T \approx \frac{n_{\text{sep}}[10^{19}\text{m}^{-3}]}{T_{\text{sep}}^2} \cdot 1000$ leads to $\alpha_{T,36021} \approx 4.0$ and $\alpha_{T,38484} \approx 7.1$. As a consequence, a change of χ correlates roughly to a similar change of α_T . To broaden this conclusion to general settings, further studies on χ are necessary.

However, heat coefficients differ between low density H-Modes (such as #36021) and standard density H-Modes (such as #38484 and 38485). For the purpose to generalize previous findings, a density scan between $n_{\text{inn}} = 2.0$ and $5.0 \cdot 10^{19} \text{ m}^{-3}$ with equal heating between electrons and ions based on χ and D of discharge #36021 is performed. The results are depicted in Fig. 5.14.



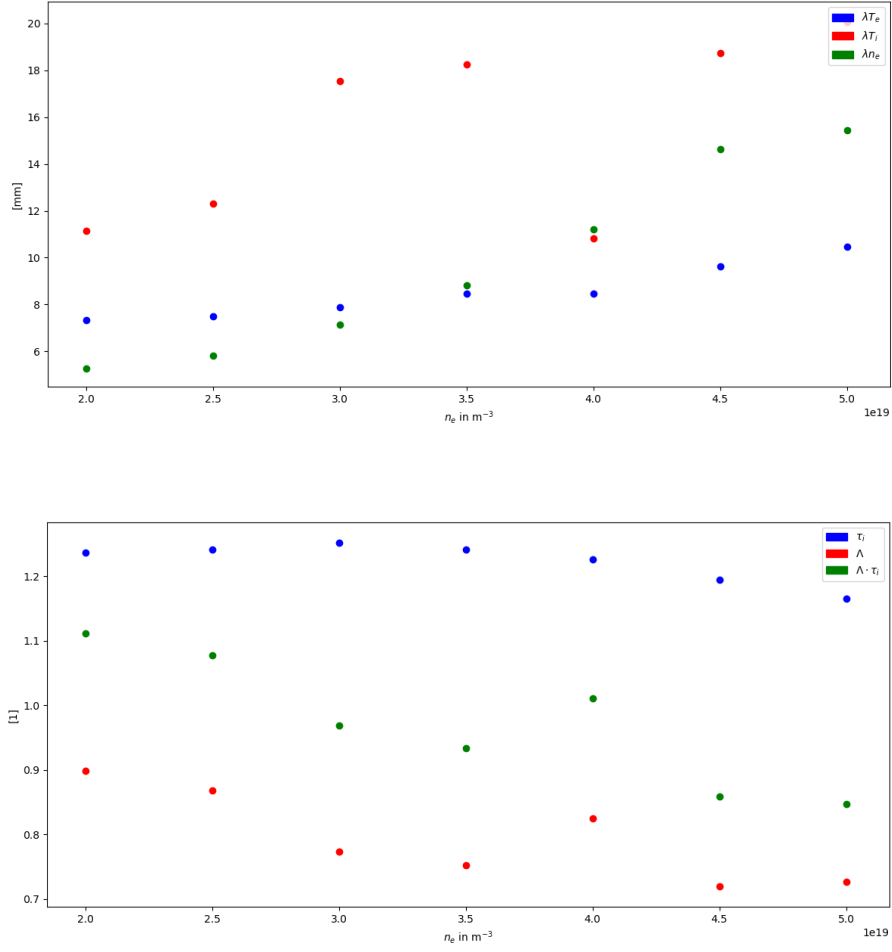


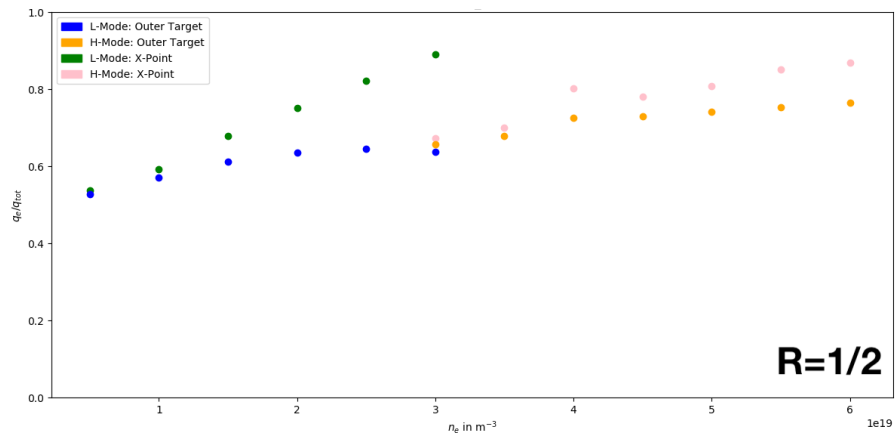
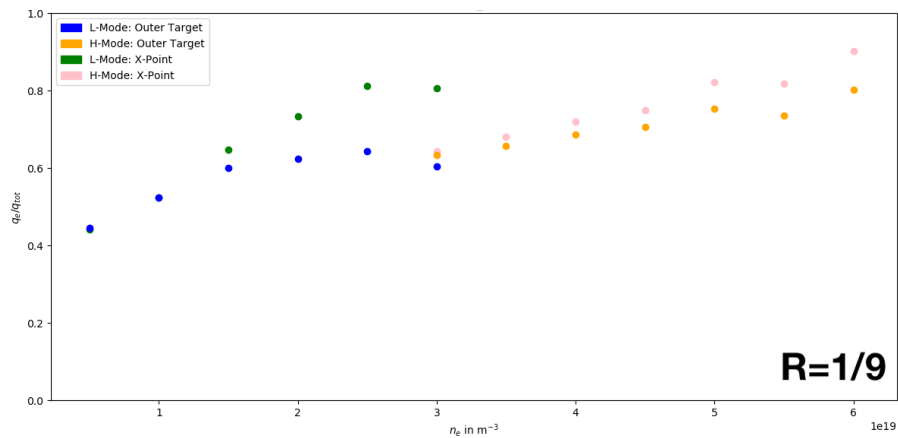
Figure 5.14: Plots of an H-Mode density scan conducted with heat coefficients based on the low density H-Mode # 36021. All plots show equal heating.

Again, no heat transport between electrons and ions within the numerical error is identified. Also, $T_i > T_e$ yields for all densities. In addition to that, the evolution of the different decay lengths is similar to the previous simulations. Lastly, the product $\tau_i \cdot \Lambda$ remains close to one.

Thus, the results prevail whether or not simulations are based on χ for low density H-Modes or standard density H-Modes. Consequently, the previous results are valid for a variation of separatrix density in H-Modes.

5.2.5 Heat transport in the SOL

After having analysed the heat flux at the separatrix, this section focuses on the heat transport in the scrape-off layer. In the SOL parallel heat fluxes dominate. This is due to the fact that heat and particles are transported parallel to magnetic field lines with the target plates as sinks. In the SOL, electron and ion heat fluxes are compared at the X-Point and at the outer target. Again, density scans at different heating ratios are compared.



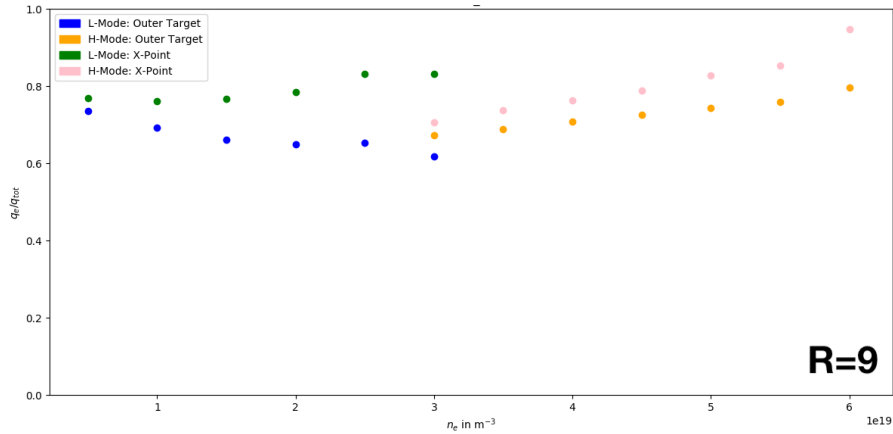


Figure 5.15: Comparison of the ratio between parallel electron and total heat flux. $q_{tot} = q_e + q_i$.

Fig. 5.15 shows that at both the X-Point and the outer target electron heat fluxes dominate. This means that on their way from the separatrix to the X-Point, electrons are heated by ions independent of their temperature at the inner simulation boundary or at the separatrix, even though the heat flux at the separatrix strongly depends on the ratio. This is valid for both L-Modes and H-Modes. Even in the case of strong ion heating ($R = 9$), more than half of the heat flux is in the electrons. The higher the density, the higher the percentage of heat flux in the electrons.

As a conclusion it can be stated, that the heat flux is mainly transported through electrons in the scrape-off layer.

5.2.6 Conclusion on heat flux behaviour in the edge

It can be concluded that the heat transport within the confinement region is not largely affected by the exchange term. Especially at typical densities of transitions between L-Mode and H-Mode ($n = 1.5 \cdot 10^{19} m^{-3}$) and at H-Mode to L-Mode back-transition ($n = 3.0 \cdot 10^{19} m^{-3}$), the influence is constrained. However, at the separatrix, ion temperature always dominates. Nevertheless, the product $\Lambda \cdot \tau_i$ is always close to one. On the other hand, in the scrape-off layer the heat flux is dominated by electrons. Therefore, q_i is transported by electrons. At the target, q_e always dominates.

Chapter 6

Conclusion

Understanding the correlation of separatrix density with turbulence parameters and electron-ion heat exchange is crucial to allow for highest possible density operation. This in turn is believed to lead to high core parameters such that the triple product is increased and therefore the likelihood of a commercial fusion reactor is improved.

Regarding the edge turbulence parameter α_t , it was shown that this parameter has an influence on pedestal and core confinement. However, this influence is neither limited to n nor T . Employing one parameter as an approach to identify the extend of the degradation of the pedestal pressure and core confinement is not successful.

The classification of the four phases developed to describe the H-Mode density limit by *Bernert* is compared to the boundary lines of turbulence by *Eich/Maunz* and show a high level of consistency. However, due to poor resolution of Thomson scattering employed to measure n_e and T_e (300 ms), further studies with higher resolution, such as Helium beam data, are proposed.

A general difficulty of validating edge turbulences is missing information on ion temperatures. In particular here, density scans were studied. These extensive density scans and the resulted modelled heat transport with EMC3-Eirene did not reveal a significant influence of the exchange term on the ratio of T_e/T_i . While ion temperature at the separatrix dominate, electrons are heated by ions in a way that at the target, electrons

dominate. A major conclusion of this work is that for typical parameters scanned in ASDEX-Upgrade discharges, the product $\frac{T_{i,sep}}{T_{e,sep}} \cdot \frac{\lambda_{pe}}{\lambda_{pi}}$ stays close to one. It is therefore of highest interest since this assumption was used in physics assumptions describing operational boundary lines. These findings are valid for both L-Modes and H-Modes and for typically accessed density ranges.

Appendix A

List of discharges used

A.1 List of discharges used in chapter 2.6.2

33063, 33064, 34275, 34276, 34277, 34338, 34339, 34610, 34825, 34973, 35869, 37624, 37625, 37919, 38114

A.2 List of discharges used in chapter 3.2

35842, 35843, 37896, 34825, 38410, 38402, 34321, 34322, 38427, 38428, 37917, 38430, 37919, 34337, 34338, 34339, 34347, 37897, 35900, 36109, 37457, 37458, 37459, 38484, 38485, 36449, 36450, 36451, 36452, 36454, 36455, 35457, 35459, 35460, 37514, 32920, 37021, 37023, 37024, 34465, 37027, 38565, 35869, 38110, 38429, 36020, 36021, 37046, 38589, 33474, 38607, 30416, 38609, 32291, 38614, 38105, 38106, 36573, 36574, 38608, 37623, 37624, 37625, 33029, 37638, 33033, 33037, 33052, 33053, 33054, 33055, 33056, 33057, 33058, 33059, 33060, 34091, 34610, 34613, 36165, 36189, 36190, 34277, 37863, 35695, 35701, 37750, 37242, 37243, 37245, 37246, 31624, 38293, 38296, 38307, 31654, 36279, 36280, 36281, 36282, 37025, 37858, 34275, 34276, 37861, 38375, 38389, 36342, 36343, 36345, 36346, 38397, 38398, 38399

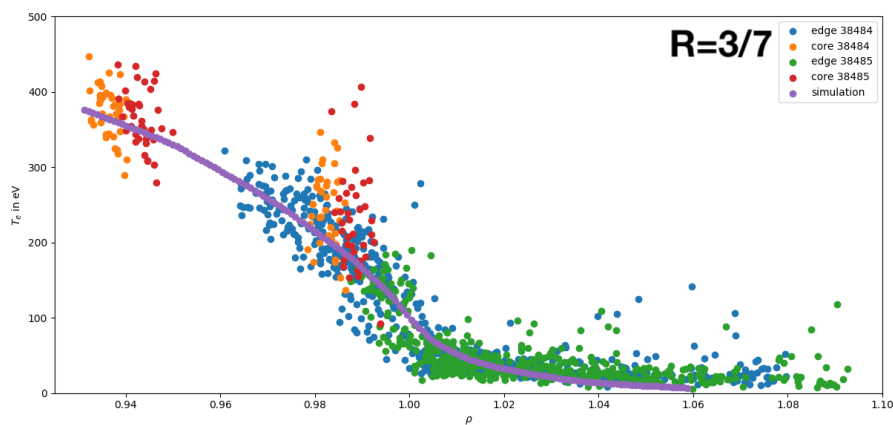
A.3 List of discharges used in chapter 4.2

28728, 29809, 29810, 34275, 34276, 34277, 34610, 34966, 34973, 38399, 38429,
38484, 38485

Appendix B

Additional plots of heat flux analysis in the edge

B.1 Determining heat and diffusion coefficients



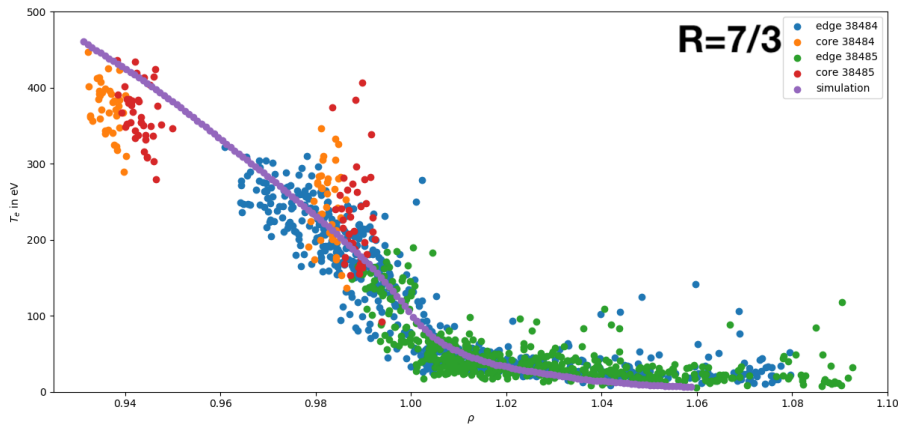


Figure B.1: Heat coefficients concerning electron temperature.

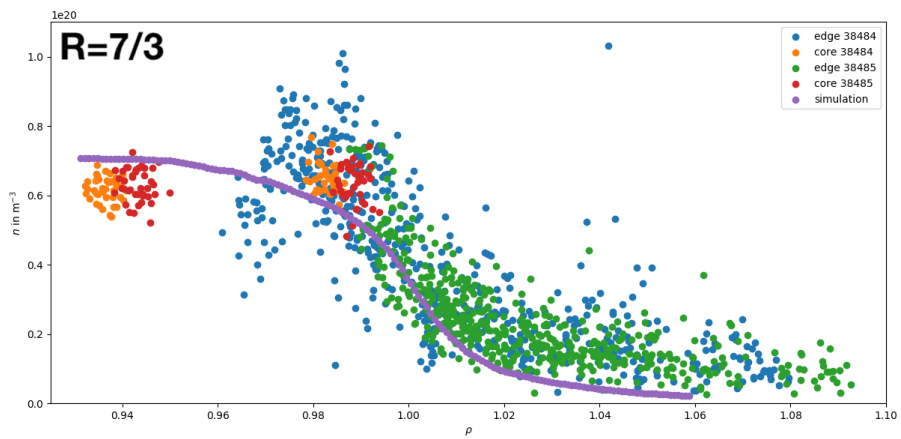
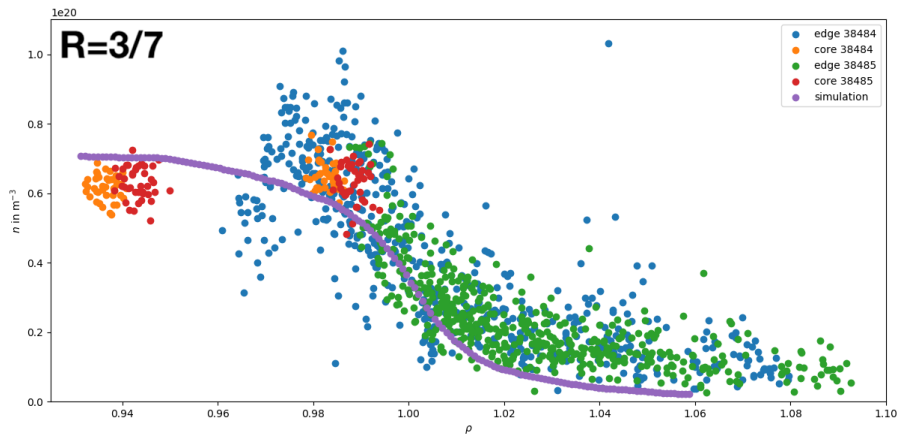


Figure B.2: Heat coefficients concerning electron density.

B.2 Heat transport at the separatrix

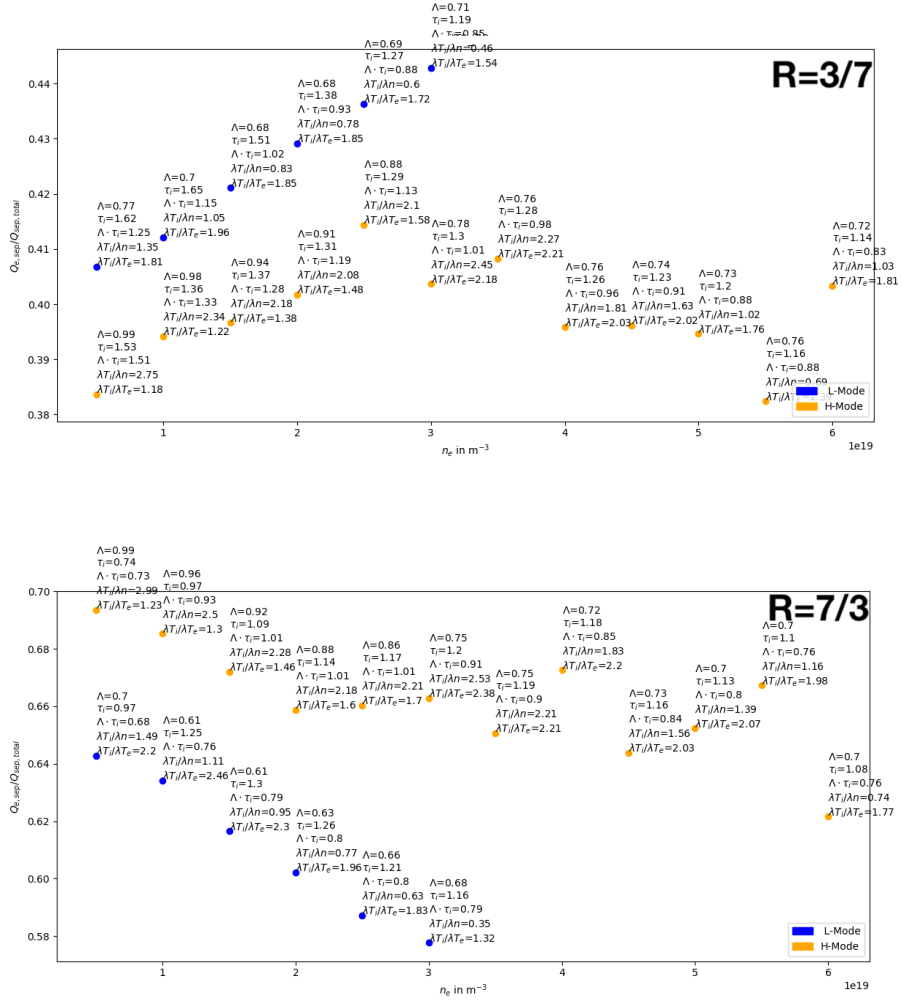


Figure B.3: Heat transport at the separatrix.

B.3 Separatrix temperature

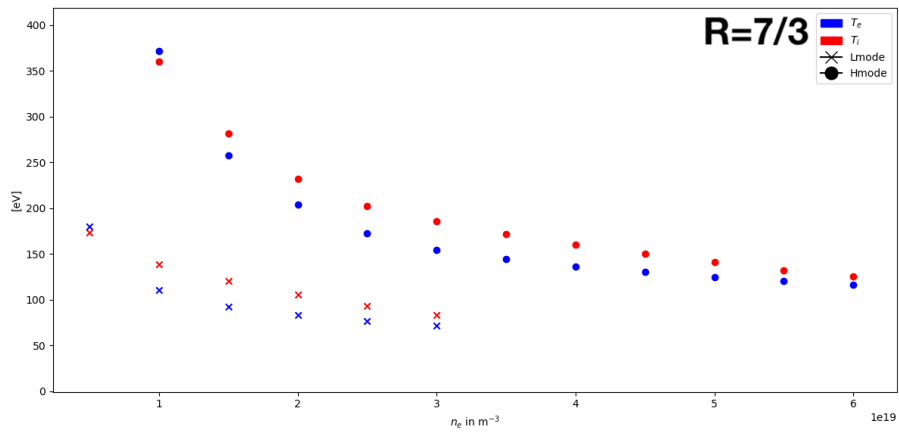
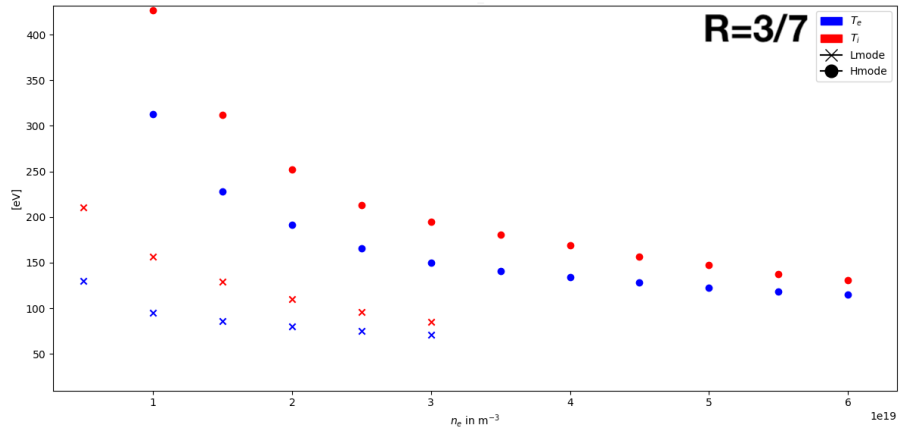


Figure B.4: Separatrix temperature.

B.4 Decay lengths

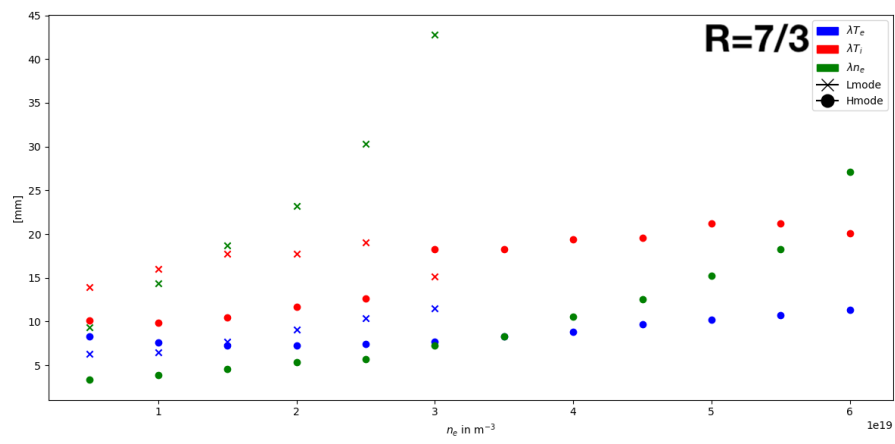
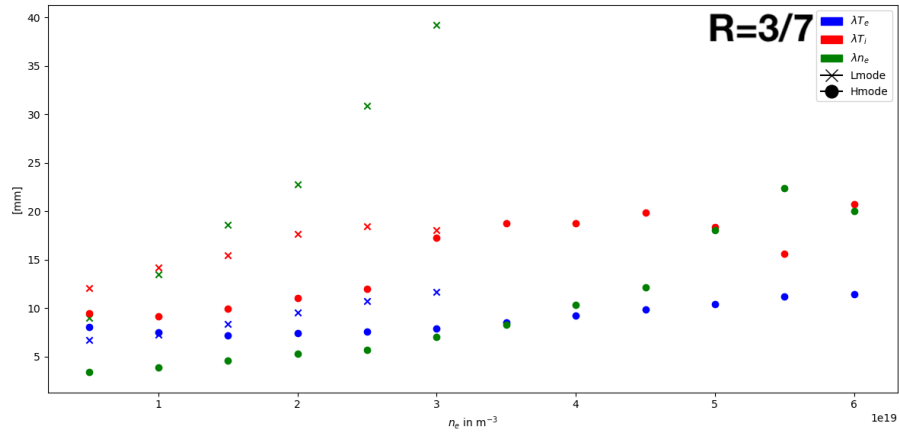


Figure B.5: Decay lengths.

B.5 Ratios of temperatures and temperature decay lengths

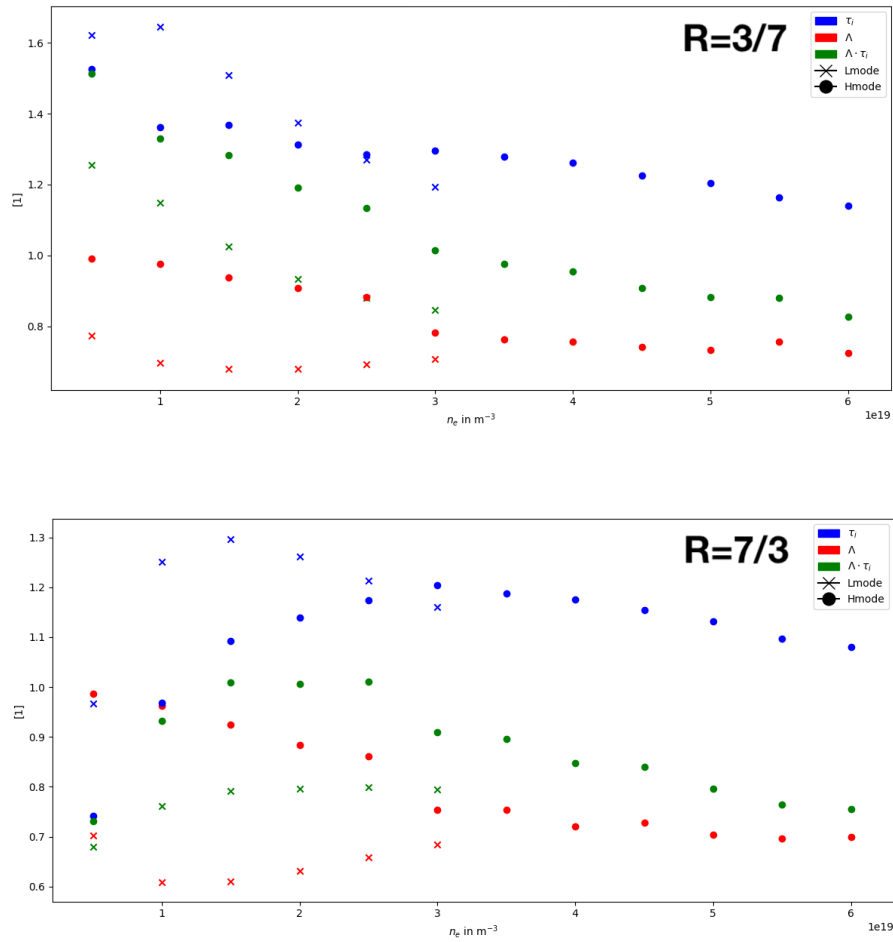


Figure B.6: Ratios of temperatures and decay lengths.

B.6 Heat transport in the SOL

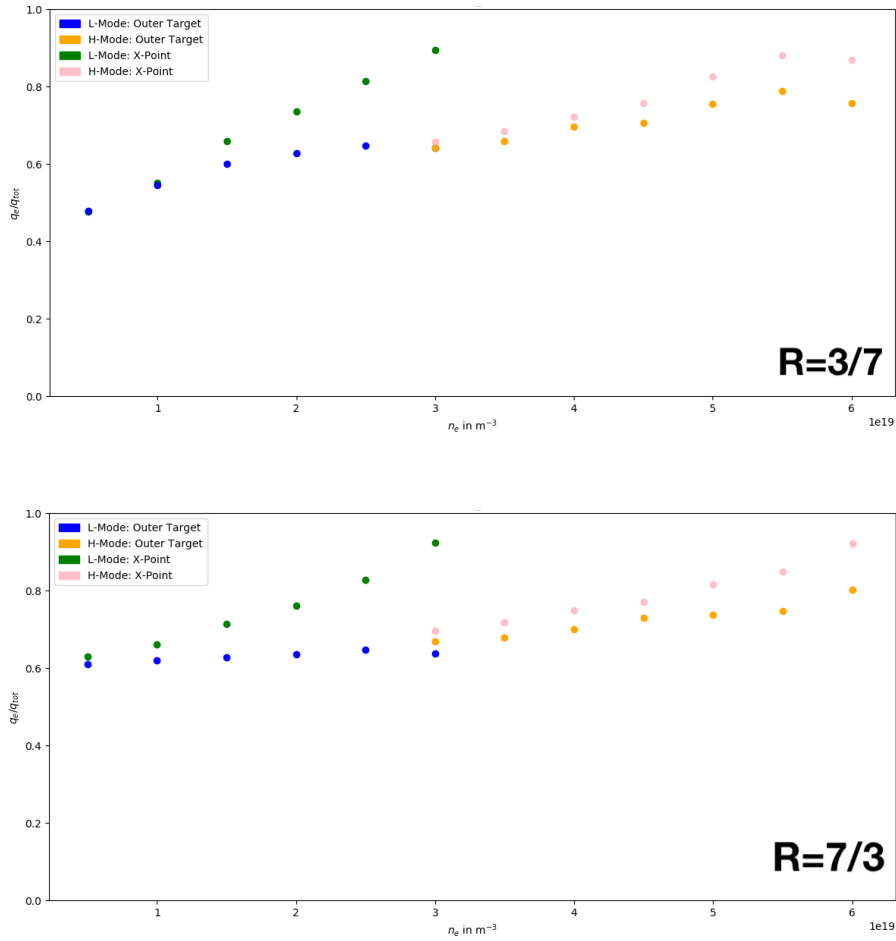


Figure B.7: Heat transport in the SOL.

Acknowledgements

This thesis is dedicated to my friend *Gerrit*, a talented and bright physicist, without whom I would have never studied physics, but left us way too early.

Special thanks to Prof. Jochum and Prof. Neu who made this special cooperation between the University of Tübingen and the IPP happen by their effort. A big thank you to Thomas Eich und Dominik Brida, who gave their help, advice and explanations without hesitation. Additionally, I thank Matthias Bernert for his help understanding his concept of the phases presented in chapter 4. I also thank the entire ASDEX Upgrade team for providing me with the infrastructure and help necessary to conduct this research. Lastly, I thank my friend Misha for proof-reading this thesis on short notice and giving me helpful linguistic tips.

Bibliography

- [1] J.D. Lawson. Some criteria for a useful thermonuclear reactor, 1993.
- [2] U. Stroth. *Plasmaphysik*, volume 7. 2557.
- [3] W. Demtröder. *Experimentalphysik IV - Kern- und Teilchenphysik*. 2017.
- [4] M. Kaufmann. *Plasmaphysik und Fusionsforschung*. 2019.
- [5] Ph. Sauter. *Influence of the heating method on power load profiles in the divertor of ASDEX Upgrade*. Bachelor thesis, Universität Tübingen, 2020.
- [6] J. Ongena, R. Koch, R. Wolf, and H. Zohm. Magnetic-confinement fusion. *Nature Physics*, 12(5):398–410, 2016.
- [7] A. Bovet. *Suprathermal ion transport in turbulent magnetized plasmas*. Phd thesis, École Polytechnique fédérale de Lausanne, 2015.
- [8] B. Sieglin. *Experimental Investigation of Heat Transport and Divertor Loads of Fusion Plasma in All Metal ASDEX Upgrade and JET*. PhD thesis, Technische Universität München, 2014.
- [9] S. I. Krasheninnikov and A. S. Kukushkin. Physics of ultimate detachment of a tokamak divertor plasma. *Journal of Plasma Physics*, 83(5), 2017.
- [10] M. Keilhacker, Wagner, F, G. Becker, K. Behringer, D. Campbell, A. Eberhagen, W. Engelhardt, G. Fussmann, O. Gehre, J. Gernhardt, G. v. Gierke, G. Haas, M. Huang, F. Karger and Z. Yu, O. Kluber, M. Kornherr, K. Lackner, G. Lisitano, G. G. Lister, H. M. Mayer, D. Meisel, E. R. Müller, H. Murmann, H. Niedermeyer, W. Poschenrieder, H. Rapp, H. Bohr, F. Schneider, G. Siller, E. Speth, A. Stabler, K.

- H. Steuer, G. Venus, O. Vollmer. Regime of Improved Confinement and High Beta in Neutral-Beam-Heated Divertor Discharges of the ASDEX Tokamak. *Physical Review Letters*, 49(19):1408–1412, 1982.
- [11] H. Wilson. Edge localized modes in tokamaks. *Fusion Science and Technology*, 57(2 T):174–182, 2010.
- [12] R.E. H.; Clark and D. Reiter. *Nuclear Fusion Research: Understanding Plasma-Surface Interactions*. Springer Science and Business Media, 2006.
- [13] ITER Physics Expert Groups on Confinement and Transport. ITER Physics Expert Groups on Confinement and Transport and Confinement Modelling and Database. *Nuclear Fusion*, 39(Chapter 2: Plasma confinement and transport):2175, 1999.
- [14] D. Silvagni. *Experimental power exhaust studies of the improved confinement regime at the ASDEX Upgrade tokamak*. Phd thesis, Technische Universität München, 2021.
- [15] F. Troyon. Theoretical Studies of MHD Stability. *Philosophical Transactions of the Royal Society of London. Series A, Mathematical and Physical Sciences*, 322(1563):163–171, 1987.
- [16] T. Eich, P. Manz, R. J. Goldston, P. Hennequin, P. David, M. Faitsch, B. Kurzan, B. Sieglin, and E. Wolfrum. Turbulence driven widening of the near-SOL power width in ASDEX Upgrade H-Mode discharges. *Nuclear Fusion*, 60(5), 2020.
- [17] D.H Froula, S.H Glenzer, N.C. Luhmann, and J. Sheffield. Chapter 1 - Introduction. In Dustin H Froula, Siegfried H Glenzer, Neville C Luhmann, and John Sheffield, editors, *Plasma Scattering of Electromagnetic Radiation (Second Edition)*, pages 1–30. Academic Press, Boston, second edition, 2011.
- [18] I. H. Hutchinson. *Scattering of electromagnetic radiation*, pages 273–321. Cambridge University Press, 2 edition, 2002.
- [19] R. Fischer, C. J. Fuchs, B. Kurzan, W. Suttrop, and E. Wolfrum. Integrated data analysis of profile diagnostics at ASDEX upgrade. *Fusion Science and Technology*, 58(2):675–684, 2010.

- [20] A. Mlynek, G. Schramm, H. Eixenberger, G. Sips, K. McCormick, M. Zilker, K. Behler, and J. Eheberg. Design of a digital multiradian phase detector and its application in fusion plasma interferometry. *Review of Scientific Instruments*, 81(3), 2010.
- [21] J. Brenner. Purely ECR-heated H-modes in ASDEX Upgrade - modeling with TGLF the effect of EC deposition on central ion temperature. *IPP Report*, 21(1):1–9, 2020.
- [22] P.H. Goldston, R.J.; Rutherford. *Introduction to Plasma Physics*. CRC Press, 1995.
- [23] D A Frank-Kamenetskii. *Interchange or Flute Instabilities*, pages 98–100. Macmillan Education UK, London, 1972.
- [24] B. D. Scott. Drift wave versus interchange turbulence in tokamak geometry: Linear versus nonlinear mode structure. *Physics of Plasmas*, 12(6):1–23, 2005.
- [25] B. D. Scott. Tokamak edge turbulence: Background theory and computation. *Plasma Physics and Controlled Fusion*, 49(7), 2007.
- [26] S. I. Braginskii. Reviews of plasma physics vol. 4. *Nuclear Physics*, 87(6):639, 1966.
- [27] T. Eich and P. Manz. The separatrix operational space of ASDEX Upgrade due to interchange-drift-Alfvén turbulence. *Nuclear Fusion*, 61(8), 2021.
- [28] P.A. Schneider. *Characterization and scaling of the tokamak edge transport barrier*. Phd thesis, Ludwigs-Maximilians-Universität München, 2012.
- [29] C. F. Jekel and G. Venter. PieceWise Linear Fitting : A Python Library for Fitting 1D Continuous Piecewise Linear Functions. 2019.
- [30] M. Bernert. *Analysis of the H-mode density limit in the ASDEX Upgrade tokamak using bolometry*. PhD thesis, Ludwig-Maximilians-Universität München, 2013.
- [31] M. Dunne and L. Frassinetti. Review of 2020 activity. In *MST1-T02*, 2021.

- [32] M. Greenwald, J. L. Terry, S. M. Wolfe, G. H. Neilson, M. G. Zweibellben, S. M. Kaye, and G. H. Neilson. A new look at density limits in tokamaks. *Nuclear Fusion*, 28(12):2207–2219, 1988.
- [33] J. Ongena, W. Suttrop, M. Bécoulet, G. Cordey, P. Dumortier, Th Eich, L. C. Ingesson, S. Jachmich, P. Lang, A. Loarte, P. Lomas, G. P. Maddison, A. Messiaen, M. F.F. Nave, J. Rapp, G. Saibene, R. Sartori, O. Sauter, J. D. Strachan, B. Unterberg, M. Valovic, B. Alper, Ph Andrew, Y. Baranov, J. Brzozowski, J. Bucalossi, M. Brix, R. Budny, M. Charlet, I. Coffey, M. De Baar, P. De Vries, C. Gowers, N. Hawkes, M. Von Hellermann, D. L. Hillis, J. Hogan, G. L. Jackson, E. Joffrin, C. Jupen, A. Kallenbach, H. R. Koslowski, K. D. Lawson, M. Mantsinen, G. Matthews, P. Monier-Garbet, D. McDonald, F. Milani, M. Murakami, A. Murari, R. Neu, V. Parail, S. Podda, M. E. Puiatti, E. Righi, F. Sartori, Y. Sarazin, A. Staebler, M. Stamp, G. Telesca, M. Valisa, B. Weysow, and K. D. Zastrow. Recent progress on JET towards the ITER reference mode of operation at high density. *Plasma Physics and Controlled Fusion*, 43(12A), 2001.
- [34] M. Greenwald. Density limits in toroidal plasmas. *Plasma Physics and Controlled Fusion*, 44(8), 2002.
- [35] K. Borrass, A. Loarte, C. F. Maggi, V. Mertens, P. Monier, R. Monk, J. Ongena, J. Rapp, G. Saibene, R. Sartori, J. Schweinzer, J. Stober, and W. Suttrop. Recent H-mode density limit studies at JET. *Nuclear Fusion*, 44(7):752–760, 2004.
- [36] M. Bernert, T. Eich, A. Kallenbach, D. Carralero, A. Huber, P. T. Lang, S. Potzel, F. Reimold, J. Schweinzer, E. Viezzer, and H. Zohm. The H-mode density limit in the full tungsten ASDEX Upgrade tokamak. *Plasma Physics and Controlled Fusion*, 57(1), 2015.
- [37] A. Pankin, D. McCune, R. Andre, G. Bateman, and A. Kritz. The tokamak Monte Carlo fast ion module NUBEAM in the national transport code collaboration library. *Computer Physics Communications*, 159(3):157–184, 2004.
- [38] F. Ryter, L. Barrera Orte, B. Kurzan, R. M. McDermott, G. Tardini, E. Viezzer, M. Bernert, and R. Fischer. Experimental evidence for the key role of the ion heat channel in the physics of the L-H transition. *Nuclear Fusion*, 54(8), 2014.

- [39] Y. Feng, F. Sardei, J. Kisslinger, and P. Grigull. A 3D Monte Carlo code for plasma transport in island divertors. *Journal of Nuclear Materials*, 241-243:930–934, 1997.
- [40] D. Reiter, M. Baelmans, and P. Börner. The eirene and B2-eirene codes. *Fusion Science and Technology*, 47(2):172–186, 2005.
- [41] D. M. Harting. *3-dimensionale Plasmarandschicht-Simulationen in unvollständig ergodisierten Magnetfeldern*. Phd thesis, Heinrich-Heine-Universität Düsseldorf, 2008.
- [42] T. Lunt, Y. Feng, D. Coster, M. Wischmeier, E. Wolfrum, R. Fischer, H. W. Müller, A. Scarabosio, and N. Hicks. Implementation and application of EMC3-EIRENE at ASDEX upgrade. *36th EPS Conference on Plasma Physics 2009, EPS 2009 - Europhysics Conference Abstracts*, 33 E1(May):414–417, 2009.
- [43] Y. Feng, M. Kobayashi, T. Lunt, and D. Reiter. Comparison between stellarator and tokamak divertor transport. *Plasma Physics and Controlled Fusion*, 53(2), 2011.